Thermal and Mechanical Properties of Hempcrete with Low-Carbon Binders: Effects of 3D Distribution and Orientation of Hemp Shivs and Microstructures of Hempcrete

Haemin Song, Siddharth Girish Nair, Taehwan Kim, Quang Dieu Nguyen, Yixiang Gan, Haiyi Zhong, Peter J. Irga, Cecilia Gravina da Rocha, Fraser R. Torpy, Sara Wilkinson, Ailar Hajimohammadi, Arnaud Castel

PII: S2352-7102(25)02100-X

DOI: https://doi.org/10.1016/j.jobe.2025.113863

Reference: JOBE 113863

To appear in: *Journal of Building Engineering*

Received Date: 12 June 2025

Revised Date: 12 August 2025

Accepted Date: 22 August 2025

Please cite this article as: H. Song, S.G. Nair, T. Kim, Q.D. Nguyen, Y. Gan, H. Zhong, P.J. Irga, C.G. da Rocha, F.R. Torpy, S. Wilkinson, A. Hajimohammadi, A. Castel, Thermal and Mechanical Properties of Hempcrete with Low-Carbon Binders: Effects of 3D Distribution and Orientation of Hemp Shivs and Microstructures of Hempcrete, *Journal of Building Engineering*, https://doi.org/10.1016/j.jobe.2025.113863.

Thermal and Mechanical Properties of Hempcrete with Low-Carbon Binders: Effects of 3D Distribution and Orientation of Hemp Shivs and Microstructures of Hempcrete

Haemin Song[1], Siddharth Girish Nair[2], Taehwan Kim[1,*], Quang Dieu Nguyen[2], Yixiang Gan[3], Haiyi Zhong[3], Peter J. Irga[2], Cecilia Gravina da Rocha[2], Fraser R. Torpy[4], Sara Wilkinson[5], Ailar Hajimohammadi[1], Arnaud Castel[2]

[1]Centre for Infrastructure Engineering and Safety, School of Civil and Environmental Engineering, University of New South Wales, Sydney, NSW 2052, Australia

[2]School of Civil and Environmental Engineering, University of Technology Sydney (UTS), Sydney, NSW 2007, Australia.

[3]School of Civil Engineering, University of Sydney, NSW 2006, Australia.

[4]School of Life Sciences, University of Technology Sydney (UTS), Sydney, NSW 2007, Australia.

[5]School of Built Environment, University of Technology Sydney (UTS), Sydney, NSW 2007, Australia.

*Corresponding author: Email: taehwan.kim@unsw.edu.au

Abstract: Hempcrete is a bio-based composite having excellent thermal insulation properties. However, the influence of low-carbon binders on the microstructural and thermal behaviour of hempcrete has not been thoroughly investigated. This study presented the effect of the mechanical and thermal properties of hempcrete using three different binders, including hydrated lime, limestone calcined clay, and alkali-activated binder. To further analyse their microstructure and gain an in-depth understanding, micro-computed tomography was employed to analyse the 3D volume fractions of different hempcrete phases and the spatial distribution and orientation of hemp shivs in hempcrete. The results demonstrated that binder selection significantly affects the hempcrete performance. Among them, hempcrete with alkali-activated binder showed 4.1 times higher compressive strength and 30.9% lower thermal conductivity compared to hydrated lime binder; this was a very interesting result because higher mechanical strength typically correlates with increased thermal conductivity. This study found that the exceptional performance was caused by a denser mortar matrix with smaller and more horizontally aligned hemp shivs than other samples.

Keywords: hempcrete; computed tomography; alkali activated material; calcined clay; thermal conductivity

Graphical Abstract

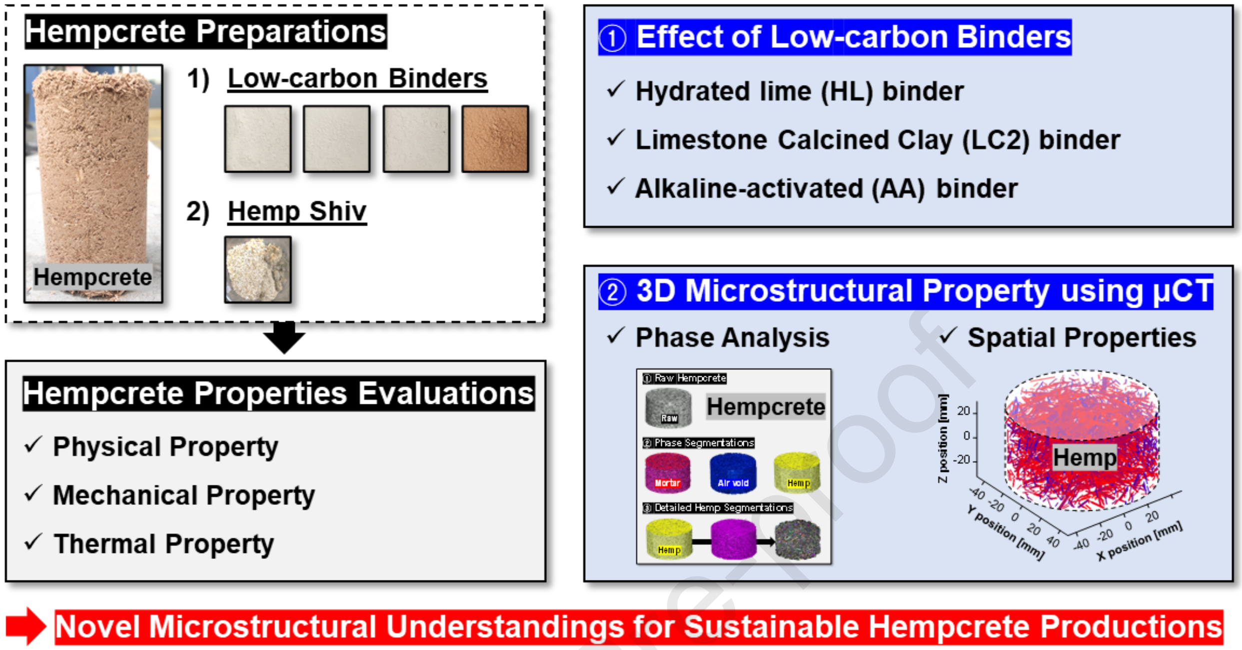

1. Introduction

According to the International Energy Agency (IEA), the building industry accounted for nearly 33% of global energy usage in 2021 [1]. As the demand for low-carbon and sustainable building materials (e.g., alternative binder [2, 3], recycled aggregate concrete [4, 5], or energy-efficient concrete [6, 7]) increases, hemp concrete (i.e., hempcrete) has gained attention as a promising bio-based material. Hempcrete consists of a hemp shiv and a binder, offering lightweight, lower CO_2 emissions, high thermal insulation, and sound-absorbing properties, making it an ideal material for energy-efficient buildings [8-10]. Furthermore, due to the high fixed carbon proportion of the hemp materials, hempcrete is considered a carbon-negative material; the inclusion of which in place of traditional concrete contributes to the reduction of atmospheric carbon throughout its lifecycle [11].

Although the type of binder plays a crucial role in determining the porosity, strength, and durability of hempcrete [12, 13], there are few comparative studies on different binder types and their performance. Hydrated lime is commonly used in hempcrete due to its widespread availability and relatively lower carbon emissions during production compared to ordinary Portland cement. Moreover, it has better compatibility with hemp shivs (the woody inner core of hemp stems) compared to Portland cement because hemp shiv absorbs considerable amounts of batching water, disrupting Portland cement hydration and hindering proper setting within the inner matrix of the composite [14-16]. Recently, limestone calcined clay (LC2) has been explored as a mineral additive due to its reduced clinker content, lower CO_2 emissions, and adequate strength development [17]. Furthermore, alkali-activated (AA) binders (e.g., geopolymers), composed of industrial by-products such as fly ash, metakaolin, and ground granulated blast furnace slag (GGBFS), have also been tested due to their high early compressive strength, low shrinkage, and reduced environmental impact [14, 18] for both hempcrete and brick applications. However, further research is required to systematically evaluate the influence of different binder systems on the physical, mechanical, thermal, and microstructure properties of hempcrete, particularly in terms of shiv-matrix interaction, pore connectivity, and long-term stability.

While numerous studies have investigated the mechanical and thermal properties of hempcrete [14, 15, 18-20], the internal microstructural characteristics of the material remain largely unexplored. Due to its high porosity and heterogeneous nature, the distribution, orientation, and pore connectivity of hemp shivs are critical factors that influence both mechanical integrity and thermal conductivity. Previous research has primarily focused on optimising binder compositions and curing conditions [14, 15, 18], yet a detailed microstructural investigation using advanced imaging techniques has never been conducted. Addressing this knowledge gap is significant to fully understand the internal structure of hempcrete and improve its practical applications.

Micro-computed tomography (μCT) is a high-resolution, non-destructive imaging technique that enables a detailed internal structural analysis of materials in three dimensions. Although widely employed in biomedical and materials science research, its application in construction materials has also recently gained attention for the assessment of cement hydration [21-23] or crack detection [24, 25]. μCT has been utilised to evaluate porosity, shiv distribution, and microstructural characteristics in various lightweight materials, including aerated concrete, foamed gypsum, and natural shiv-reinforced composites [26]. Recent studies have investigated μCT applications in hempcrete, particularly for analysing shiv orientation, pore connectivity, and shiv-binder interactions [27-29], but there are still only very limited studies that use μCT to investigate hempcrete microstructure. Notably, in a preliminary study [30], a new phase segmentation technique was developed that distinguishes complex pore phases in hempcrete, including air voids, intra-pore spaces within hemp shivs, and intra-pore spaces in mortar. This information is essential for enhancing the performance of hempcrete in sustainable construction applications.

This study demonstrates the influence of different low-carbon binders and 3D hemp properties (dimension, distribution, and orientation) on the mechanical and thermal insulation performance of hempcrete. These findings will provide new understandings into the interactions between hemp shivs and binders, which may contribute to the development of more resource-efficient hempcrete. Three types of low-carbon binder mixes were compared in this study. The first binder was reference hydrated lime. The second binder was a low-carbon binder composed of limestone, calcined clay and hydrated lime (LC2). The third binder was a calcined clay/ ground granulated blast furnace slag (GGBFS)-based alkali-activated binder, which is also a low-carbon binder. To comprehensively evaluate the properties of hempcrete, X-ray diffraction (XRD) and X-ray fluorescence (XRF) analyses were conducted to characterise the mineralogical and chemical compositions of the binders. Consequently, bulk density, compressive strength, adhesion strength, and thermal conductivity of hempcrete samples were measured to evaluate the effect of binders on hempcrete properties. All experiments relating to the μCT were carried out at the School of Civil and Environmental Engineering at the University of New South Wales.

2. Materials and Methods

2.1. Raw Materials

2.1.1. Raw Precursors and Activators

For the preparation of a calcined clay-GGBFS-based alkali-activated binder, analytical-grade sodium hydroxide (NaOH) pellets (>98.0%) and sodium silicate solution (water glass) were utilised for the activator. The sodium silicate solution contained 9.1 wt.% Na_2O, 28.9 wt.% SiO_2, and 62.0 wt.% H_2O.

Fig. 1 presents photography of the raw precursors used in this study. Hydrated lime (AHMC, Australia), calcined clay (Argeco, France), limestone (Omya, Australia), ground granulated blast furnace slag (GGBFS; Australian Steel Mill Services, Australia), and sand (Sydney sand, Australia) were used. All materials were in fine powder form, with calcined clay exhibiting a brownish colour, while hydrated lime, limestone, and GGBFS appeared white or off-white. The observed particle texture suggests a similar level of fineness across all precursors, with minor visible agglomeration.

Fig. 1. Visual inspection of raw precursors.

Table 1 summarises the chemical composition, particle size distribution, specific density, and mineral compositions of the raw precursors used in this study.

First of all, X-ray fluorescence (XRF) spectroscopy (Axios, Malvern Panalytical, United Kingdom) was used to characterise the oxide compositions of the raw precursors: hydrated lime, calcined clay, limestone, and GGBFS. Hydrated lime and limestone are composed mainly of CaO, containing 71.6% and 54.3% CaO, respectively. Calcined clay was mainly composed of SiO_2

(71.2%) and Al_2O_3 (22.5%), whereas GGBFS contained a combination of CaO (44.8%), SiO_2 (31.7%), and Al_2O_3 (12.3%). In terms of loss on ignition (LOI), limestone exhibited the highest value (42.7%), followed by hydrated lime (25.4%), mainly due to the decomposition of calcite ($CaCO_3$) and portlandite [$Ca(OH)_2$], respectively. In contrast, calcined clay (1.8%) and GGBFS (0.8%) showed significantly lower LOI values, indicating minimal mass loss under high temperatures.

The particle size distribution of the raw precursors was determined using a particle size analyser (Mastersizer 2000, Malvern Panalytical, United Kingdom). Regarding particle size distribution, the median particle size (D_{50}) of hydrated lime (19.2 μm) was larger than that of GGBFS (11.4 μm) and limestone (6.9 μm) but smaller than that of calcined clay (31.6 μm). The 90 percentile of the particle size distribution (D_{90}) values further indicated that hydrated lime had a coarser particle size distribution (286.2 μm) than calcined clay (98.7 μm), limestone (43.2 μm), and GGBFS (28.7 μm). The detailed particle size distribution of the raw precursors can be found in Appendix A.

The specific density of the precursors was measured using a nitrogen gas pycnometer (Ultrapyc 5000, Anton Paar, Austria). The final density value was obtained by averaging the last three measurements from a total of 15 repetitions, ensuring stability in the recorded data. The specific density of hydrated lime (3.02 g/cm^3) was higher than that of the other precursors, which ranged from 2.50 to 2.72 g/cm^3. Notably, limestone exhibited the lowest specific density (2.50 g/cm^3).

The mineralogical composition of the precursors was examined using powder X-ray diffraction (XRD; Empyrean 2, PANalytical, United Kingdom) with Co-Kα radiation ($\lambda = 1.79$ Å) over a 2θ scanning range of 5–60°. The quantitative phase analysis was conducted using X'pert

High Score software, which compares the measured XRD patterns with reference data from the International Centre for Diffraction Data (ICDD) [31]. Afterwards, X'pert High Score software with Rietveld refinement was used for quantitative analysis with silicon used as the external standard.

In the XRD results, hydrated lime consisted predominantly of portlandite [$Ca(OH)_2$, 67.6%], along with alite ($3CaO \cdot SiO_2$, 20.9%) and calcite ($CaCO_3$, 11.5%). Limestone powder was 100.0% calcite. According to the XRD analysis, all observed peaks matched well with the standard pattern of calcite, and no other crystalline phases were detected. Therefore, the limestone used can be considered pure $CaCO_3$ within the detection limits of the instrument. Meanwhile, calcined clay predominantly consisted of an amorphous phase (64.7%), with quartz (35.3%) as the main crystalline phase. The high amorphous content confirms its potential reactivity as a pozzolanic material in the LC2 binder. GGBFS exhibited an amorphous phase content of 99.6%, with a negligible presence of quartz (0.4%). The high amorphous content is indicative of its high latent hydraulic reactivity, making it an excellent precursor for alkali-activated binders [32].

Table 1. Summary of the characteristics of the raw precursors. Note: LOI: loss on ignition; D_{10}, D_{50}, and D_{90} were the particle sizes below which 10, 50, and 90% of the soil particles were smaller, respectively. The standard deviations of all specific densities were <0.001 g/cm^3.

Label		Hydrated lime	Calcined clay	Limestone	GGBFS
Oxides (wt%)	CaO	71.6	0.5	54.3	44.8
	SiO_2	1.3	71.2	1.1	31.7
	MgO	0.8	0.2	1.5	4.6
	Al_2O_3	0.5	22.5	0.2	12.3
	Fe_2O_3	0.3	2.3	0.2	1.1
	TiO_2	0.1	1.1	-	1.0

	SO_3	-	-	-	3.2
	LOI	25.4	1.8	42.7	0.8
Particle size (μm)	D_{10}	2.8	3.8	1.4	1.7
	D_{50}	19.2	31.6	6.9	11.4
	D_{90}	286.2	98.7	43.2	28.7
Specific density (g/cm^3)		3.02	2.55	2.50	2.72
Mineral compositions (%)	$Ca(OH)_2$	67.6	-	-	-
	$3CaO \cdot SiO_2$	20.9	-	-	-
	$CaCO_3$	11.5	-	100.0	-
	SiO_2	-	35.3	-	0.4
	Amorphous	-	64.7	-	99.6

2.1.2. Hemp Shivs

The present study utilised hemp shiv, which refers to the woody core of industrial hemp stems that remain after the retting process. The hemp hurds were obtained by using a hemp decorticator machine to separate the hemp hurds and the bast fibre from the woody core of the hemp stalk. The hemp shiv used in this study was supplied by the Australian Hemp Masonry Company (AHMC), Australia and was farmed in Tamworth, New South Wales, Australia.

The particle size distribution of hemp shivs was evaluated through their residual weight percentage using a sieving machine. A 150.0 g sample of air-dried hemp shivs was sieved three times, with each cycle lasting 10 minutes, to classify the hemp shivs based on their size and shape. **Fig. 2** illustrates the size variations of the raw hemp particles, which were separated through a sieving process. The image visually categorises the hemp particles into different size ranges, with the majority falling within the 2.36–4.75 mm (44.8%) and 1.18–2.36 mm (35.8%) size ranges, which are classified as shivs. Additionally, larger fractions (4.75–9.5 mm), including fibre-like components (marked in red), were also observed. Meanwhile, fine particles (<0.6 mm), representing dust-like fines that may influence the matrix interaction in hempcrete [18], were present in minimal amounts, accounting for only 2.5%.

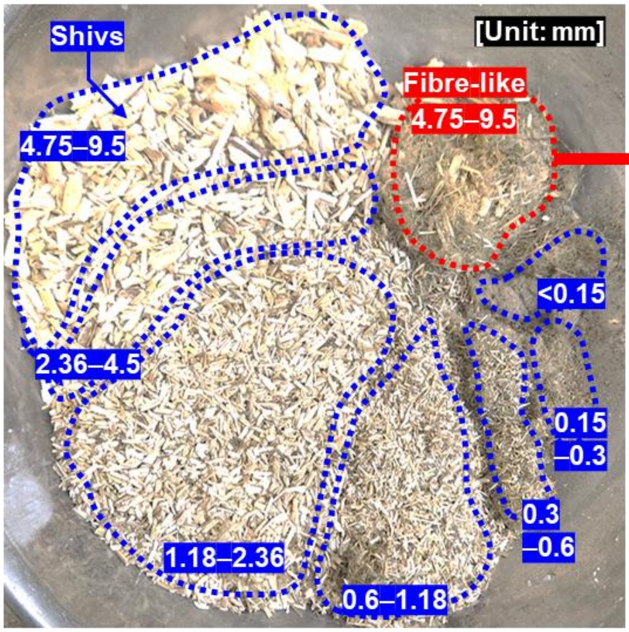

Size [mm]	Residual weight percentage [%]
>9.5	2.6 (0.8)
4.75–9.5 (Fibre-like)	1.3 (3.7)
4.75–9.5 (Shiv)	5.0 (2.4)
2.36–4.75	44.8 (8.5)
1.18–2.36	35.8 (5.5)
0.6–1.18	7.9 (0.9)
0.3–0.6	1.7 (0.4)
0.15–0.3	0.4 (0.0)
<0.15	0.4 (0.0)
Sum	100.0

Fig. 2. Size variations of raw hemp particles. Values in parentheses indicate the standard deviation from triplicate measurements.

2.2. Hempcrete

2.2.1. Sample Preparation

Table 2 outlines the mixture proportions of hempcrete samples with low-carbon different binders. Three different hempcrete (HC) samples (i.e., HC-HL, HC-LC2, and HC-AA) were prepared based on three different low-carbon binders: a hydrated lime (HL) binder, a limestone calcined clay (LC2) binder, and an alkali-activated (AA) binder. The precursor: sand: mixing solution: hemp ratio was fixed at 9.0: 5.0: 10.0: 5.0 based on the preliminary study [13, 30]. Unlike conventional Portland cement concrete, which contains incompressible constituents, hempcrete contains a compressible phase (i.e., hemp shivs [30]), the compacted density of which varies depending on the degree of compaction. Therefore, the mixing ratio is expressed in units of kg of each component, as in previous studies [13, 33, 34].

HC-HL included 100% hydrated lime, HC-LC2 contained 50.0% hydrated lime, 33.3% calcined clay, and 16.7% limestone, while HC-AA precursor composition was 70.0% calcined clay and 30.0% GGBFS. As a mixing solution, HC-HL and HC-LC2 used water, while HC-AA used an alkaline activator. Before this, the alkaline activator was prepared by dissolving NaOH pellets and water glass with the weight ratio in the mixing table. Its silica modulus (i.e., SiO_2/Na_2O mass ratio in the activator) and the alkali dosage (i.e., the mass ratio of Na_2O in the activator to the precursors) were 1.1 and 10.5%, respectively.

Table 2. Mix proportions of hempcrete in wt.%. Note: (HC) hempcrete, (HL) hydrated lime binder, (LC2) limestone calcined clay binder, and (AA) alkali-activated binder.

Label			HC-HL	HC-LC2	HC-AA
Mortar	Precursor	Hydrated lime	31.0	15.5	-
		Calcined clay	-	10.2	21.7
		Limestone	-	5.3	-
		GGBFS	-	-	9.3
	Sand		17.2	17.2	17.2
	Mixing solution	Water	34.5	34.5	19.9
		NaOH	-	-	2.8
		Water glass	-	-	11.8
Hemp			17.2	17.2	17.2
Sum			100.0	100.0	100.0

The mixing solution required for the chemical reactions of the precursors can be depleted due to the high initial water content (INC) of hemp shivs (see **Fig. B1**). Thus, the present study mixed hempcrete composites in two steps using a 70 L electric pan mixer. First, to achieve a saturated surface dry (SSD) condition of hemp shivs, they were mixed for 1 minute with a portion of the mixing solution equivalent to their INC. Second, after adding the remaining solution, the dry-mixed precursors and sand, they were mixed for an additional 2 minutes.

The fresh hempcrete mixtures were cast into cylindrical moulds (100.0 mm in diameter and 200.0 mm in height) for compressive strength, bulk density, thermal conductivity, adhesion measurements, and μCT analysis. A 2.7 kg compacting hammer was applied five times per layer to ensure uniform compaction across the three layers. Then, all samples were demoulded after 24 hours of initial curing and subsequently stored under controlled conditions at 23 ± 2°C and 55 ± 3% relative humidity until specific testing dates.

In this study, the setting times of the mixtures were not quantitatively measured. However, visual observations during mixing and casting showed no abnormal quick-setting in any of the binders. All mixtures maintained sufficient workability throughout the mixing and casting process, and after one day of curing, the specimens were sufficiently hardened to allow demolding without surface damage.

2.2.2. Physical, Mechanical, and Thermal Properties

All tests for bulk density, adhesion, compressive strength, and thermal conductivity were performed on triplicate hempcrete samples (100.0 mm in diameter and 200.0 mm in height), and their mean values and standard deviations were recorded.

The bulk density of the hempcrete samples was determined by dividing their measured weight at 7, 14, 21, and 28 days after manufacture by their respective volume (100.0 mm in diameter and 200.0 mm in height).

The adhesion test was conducted using a pull-off adhesion tester (Positest AT) to evaluate the interfacial bond strength on the surface of the hardened hempcrete [4]. An adhesion testing dolly was attached to the sample surface using a high-strength two-part epoxy resin, and tensile load was applied perpendicular to the surface until failure occurred. The maximum force recorded at detachment was used to calculate the adhesion strength.

The compressive strength was evaluated at 7, 14, 21, and 28 days under displacement control. A thin rubber sheet was placed between the sample and press plates to reduce interfacial gaps and ensure uniform load distribution.

The thermal conductivity of the hempcrete samples was evaluated using a Hot Disk thermal constant analyser (TPS 500S, Hot Disk AB, Sweden), which operated based on the transient plane source (TPS) method. Measurements were performed with an input power of 250 mW and a measurement time of 640 seconds [35, 36]. This method allows for accurate characterisation of low-conductivity and heterogeneous materials, such as hempcrete [37], by minimising heat losses and capturing the time-dependent temperature response of the specimen.

2.2.3. 3D Microstructural Property using μCT

Using the μCT technique, 3D phase identification was performed on the hempcrete samples incorporating different low-carbon binders to visually assess three internal components (air voids, hemp, and mortar) and identify the spatial distribution and orientation of hemp shivs within the hempcrete matrix.

To ensure that the internal moisture within the hemp had fully evaporated and that the chemical reactions of the binders were complete, approximately 72-day cured samples were selected for μCT measurements. Each hempcrete sample was mounted on a rotational stage and rotated 360° during scanning. The central region of the specimens (100.0 mm in diameter and 50.0 mm in height) was scanned under an applied current of 78 μA at 80 kV. The acquisition process lasted 3.5 hours, generating 2,520 projections in circular mode. Then, these X-ray projection data were reconstructed to obtain a 3D grayscale image, yielding a tomographic resolution of 44.7 μm/pixel.

Fig. 3 presents the segmentation process of the hempcrete samples using 3D visualisation software (Avizo, Thermo Fisher Scientific, United States). Initially, the raw 2D tomographic sliced images were processed using a median filter. A masking image was then generated to eliminate the exterior region of the hempcrete samples.

To identify the three phases within the hempcrete samples, two thresholding values (i.e., air void-to-hemp and hemp-to-mortar) were required. However, due to the relatively low proportion of air voids compared to the other phases, direct threshold computation from the colourmap histogram of the entire sample was not feasible. Thus, based on the author's preliminary study [30], three subvolumes containing well-distributed air void, hemp, and mortar phases were selected from the top, middle, and bottom sections of the samples as shown in **Fig. 3**. Each subvolume (0.45 × 0.45 × 0.45 mm^3) exhibited distinct air void phases in the histogram, enabling threshold computation after deconvolution using MATLAB software.

The first thresholding value (air void-to-hemp) was determined as the intersection point between the air void and hemp phases (see the left blue vertical line at the deconvolution stage in **Fig. 3)**. However, due to the heterogeneity of hempcrete, an interphase between the hemp and mortar phases was observed. Consequently, the second thresholding value (hemp-to-mortar) was computed as the average of two intersections, including the intersection point between the hemp phase and interphase and another point between the interphase and mortar phases. (see two black vertical lines and the right blue vertical line at the deconvolution stage in **Fig. 3)**

The averaged thresholding values derived from the three subvolumes were subsequently applied to the entire hempcrete sample segmentation. Finally, the volume fractions of the three phases (air voids, hemp, and mortar) were calculated.

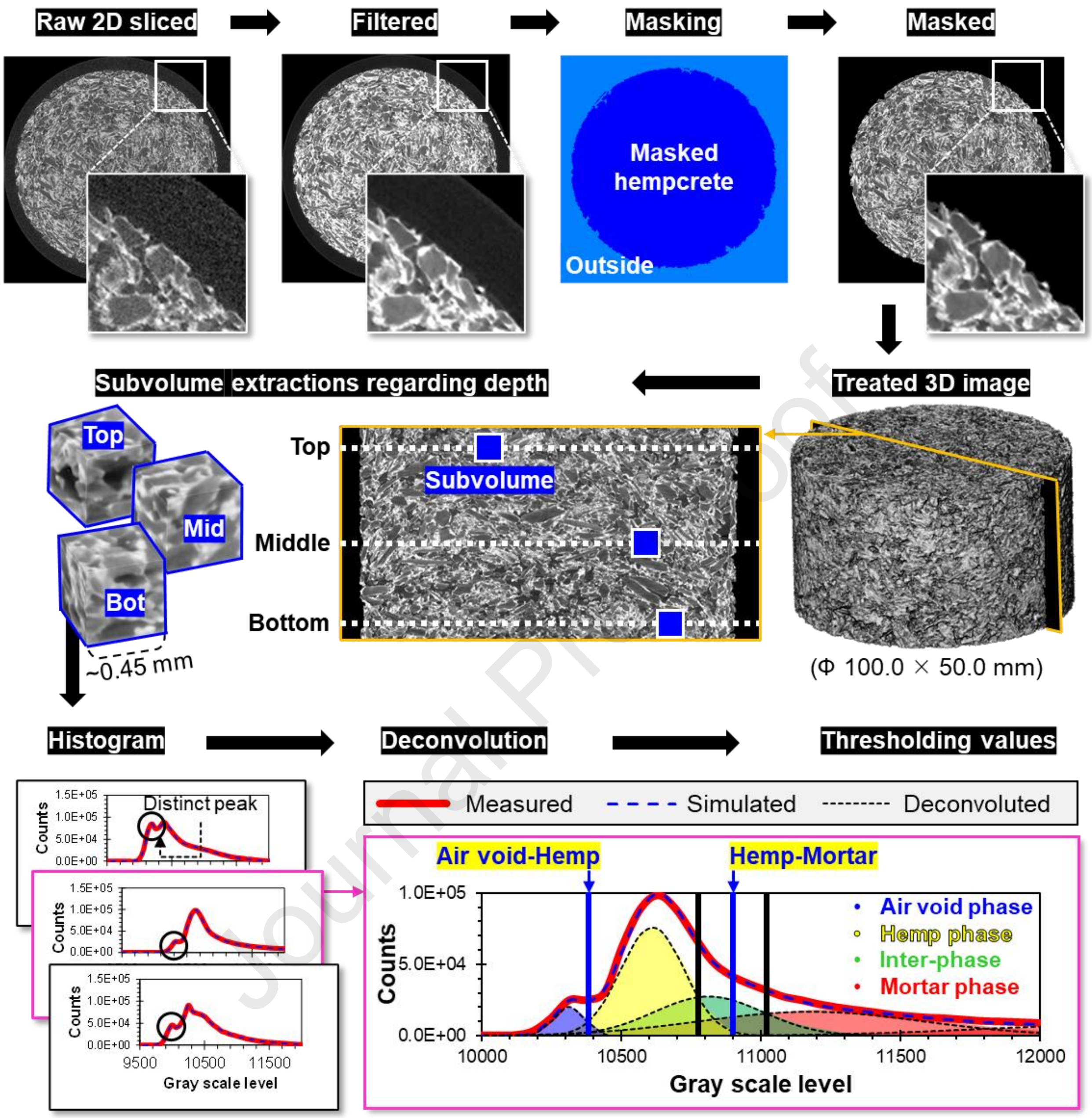

287

288 **Fig. 3.** Hempcrete segmentation using Aviso and MATLAB software.

289

290 **3. Results**

291 **3.1. Physical, Mechanical, and Thermal Properties of Hempcrete**

Fig. 4 presents the material properties of hempcrete samples incorporating three different binders, including bulk density, adhesion, compressive strength, and thermal conductivity. Significant differences were observed across treatment types, with differences observed across all tests, including physical, mechanical, and thermal properties of hempcrete. The statistical significance of the experimental data was also analysed, and sufficient significance was obtained. Details are in Appendix C.

First, **Fig. 4** (a) presents the bulk density of the hempcrete samples over time. HC-AA exhibited the highest bulk density, whereas HC-LC2 had the lowest. All samples experienced a reduction in bulk density during the curing period, primarily due to moisture loss. After 28 days, HC-HL exhibited the highest weight loss (15.2%), followed by HC-AA (10.4%) and HC-LC2 (9.9%). The rapid drying observed in HC-HL may be attributed to the higher permeability of the hydrated lime binder, which facilitates faster water evaporation and promotes carbonation reactions.

The bulk density of the hempcrete samples decreased due to moisture evaporation during the initial curing period, but the weight loss rate was minimal after approximately 21 days, indicating that the moisture content has been stabilised. The residual moisture during the initial curing stage is closely related to the hydration and hardening of the binder, which can affect the compressive strength and adhesion. In addition, since water has a higher thermal conductivity than hempcrete, the presence of free water can affect the measured thermal conductivity. To minimise this effect and ensure that the test results reflect the unique properties of hardened hempcrete, the compressive strength, adhesion, and thermal conductivity were evaluated at 28 days in this study, when most of the moisture-induced changes have stabilised.

Next, in **Fig. 4** (b), the adhesion strength of HC-AA was stronger compared to that of HC-HL and HC-LC2. The adhesion between the hemp shiv and the mortar is a significant factor influencing the mechanical integrity of hempcrete. The adhesion strength is primarily affected by the interfacial bonding between the hemp surface and the mortar, which can be weakened by the swelling and shrinkage of hemp shivs due to their hygroscopic characteristic [38]. Furthermore, hemp shivs can deform depending on their moisture content, affecting the bond strength with the surrounding matrix [14]. Moreover, the notably higher adhesion in HC-AA could be attributed to its alkaline environment. For example, previous studies have shown that alkaline solutions (e.g., NaOH or water glass) can partially delignify hemp [30], leading to changes in surface morphology and improving matrix adhesion [14]. Thus, improved adhesion in HC-AA might correlate with higher alkalinity and potential surface modifications of hemp shivs.

Fig. 4 (c) illustrates the 28-day compressive strength of the hempcrete samples. The reference hempcrete achieved ~ 0.16 MPa. The compressive strength of HC-LC2 was ~ 60% higher at ~ 0.26 MPa, highlighting the synergy benefits of limestone and calcined clay in a lime-based system. HC-AA exhibited the highest compressive strength, reaching 0.65 MPa, which is approximately 4.1 times higher than that of the reference hempcrete (HC-HL). Previous studies have also reported that hempcrete generally exhibits low compressive strength (<1 MPa) [20], which aligns with the current findings. A high hemp shiv ratio (17.2 wt% in **Table 2**) might affect mechanical performance due to the inherently weak mechanical properties of hemp shivs. Moreover, although hemp absorbed a significant amount of mixing solution (see **Fig. B1**), the overall water-to-precursor ratio in the mixtures remained high (34.5/31.0 = 1.11 in **Table 2**), contributing to the low mechanical strength of the samples.

In **Fig. 4** (d), the 28-day thermal conductivity of the hempcrete samples varied depending on the binder type. HC-AA exhibited thermal conductivity values that were 15.0–30.9% lower than those of HC-LC2 and HC-HL. However, preliminary tests on mortar samples using the same binders and experimental methods (see **Fig. C1**) showed a different trend: the thermal conductivity of the HL mortar was 3.44 ± 0.21 W/mK, the LC2 mortar was 2.84 ± 0.17 W/mK, and the AA mortar was 3.18 ± 0.22 W/mK. It should be noted that the mortar thermal conductivity trends did not agree with those of hempcrete samples. This discrepancy suggests that other hemp-related factors have a more dominant effect on the thermal performance of hempcrete than the binder alone. This counterintuitive correlation will be further discussed in Section 4.2.

In summary, among the hempcrete samples, HC-AA exhibited the highest density, adhesion strength, and compressive strength, suggesting its potential for enhanced structural performance, while also demonstrating the lowest thermal conductivity, indicating that it has superior insulating capability. These results are discussed in Section 4.2.

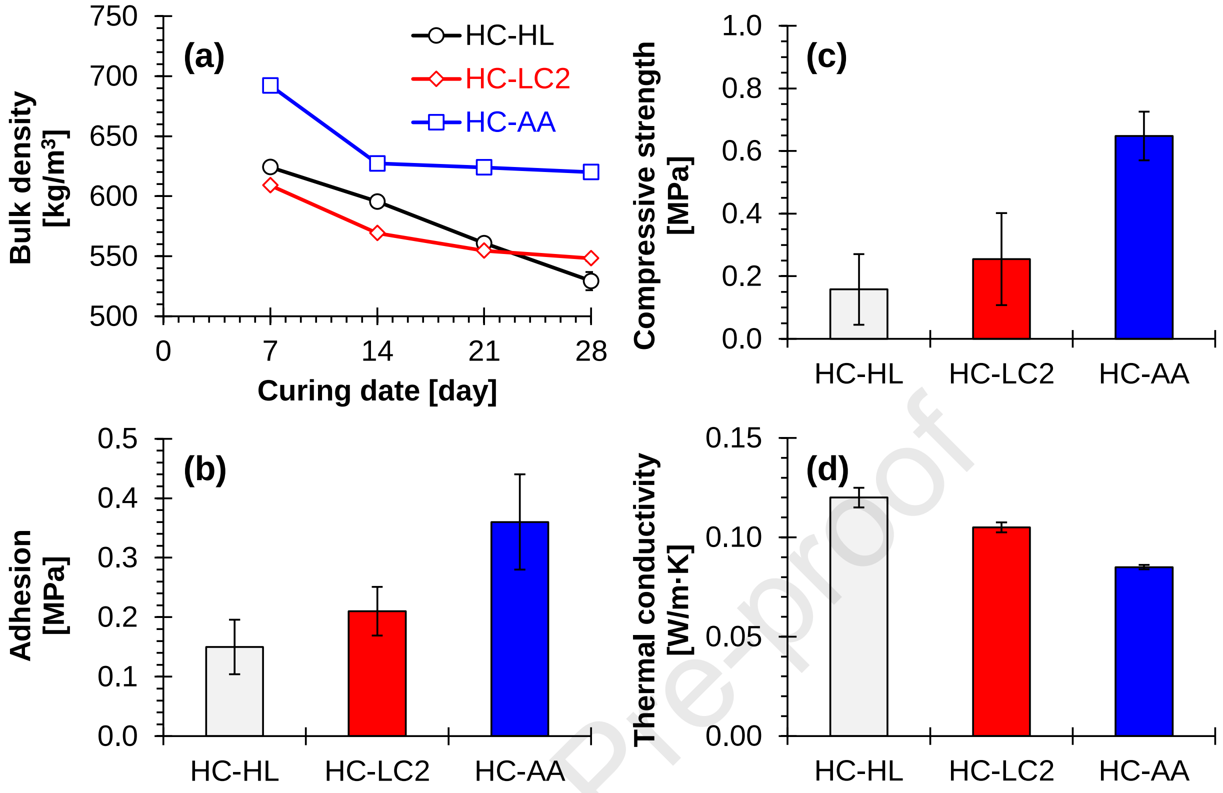

Fig. 4. Properties of hempcrete samples: (a) bulk density, (b) adhesion at 28 days, (c) compressive strength at 28 days, and (d) thermal conductivity at 28 days.

3.2. 3D Microstructural Property using μCT

3.2.1. Phase Segmentations

Fig. 5 presents the 3D volume reconstructions and 2D sliced tomograms of hempcrete samples obtained through μCT analysis. The top row shows the 3D visualisations, while the bottom row displays the corresponding X-Y cross-sectional images. The grayscale intensity in these images represents the X-ray transmittance, where denser regions appear brighter, while less dense regions, such as air voids and hemp shivs, appear darker [30].

By observing the variation of grayscale in **Fig. 5**, it is clear that the different binder types had a noticeable influence on the internal structure of hempcrete. The HC-HL and HC-LC2 samples exhibited distinct phase separation, with well-dispersed hemp shivs and visible pore structures. In contrast, the HC-AA sample appeared denser, with reduced porosity and a more homogeneous distribution of phases. This suggests that the alkali-activated binder (HC-AA) facilitated better matrix densification compared to hydrated lime (HC-HL) and LC2-based binders (HC-LC2). Furthermore, the relatively bright regions in HC-AA may indicate improved binder densification, correlating with the observed higher bulk density [see **Fig. 4 (a)**] and better mechanical performance [see **Fig. 4 (c)**] compared to other samples.

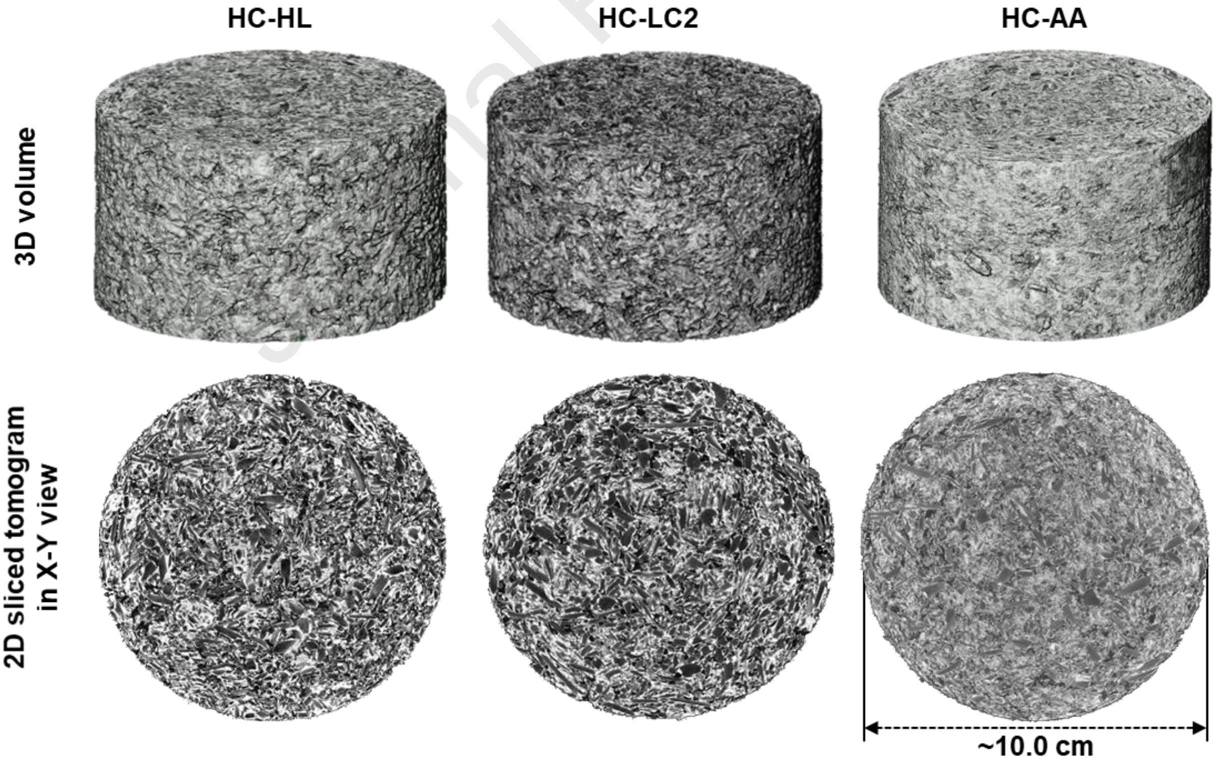

Fig. 5. 3D volume and 2D sliced tomogram of hempcrete samples.

Fig. 6 presents the raw 2D tomograms (left column) and segmented images (right column) of hempcrete samples in the Y-Z view, obtained through μCT analysis. The segmentation process was performed using Avizo software following the methodology described in **Fig. 3**, which involved subvolume extraction, histogram analysis, and deconvolution methods. The internal components were categorised into air voids (blue), hemp (yellow), and mortar phase (red), providing insights into their distribution and interaction within the hempcrete matrix.

In the raw tomograms, distinct differences in the internal structures of the three hempcrete samples are evident. The HC-HL and HC-LC2 samples were highly porous, with well-defined hemp shivs and air voids dispersed throughout the binder matrix. In contrast, the HC-AA sample appears more compact, with fewer visible pores and smaller hemp shivs, indicating a denser microstructure. Additionally, the cross-section images show that the HC-HL and HC-LC2 samples contain a significant proportion of air voids, contributing to their highly porous structure. The hemp shivs were well-distributed, while the mortar phase formed the continuous binding matrix. Comparatively, the HC-AA sample exhibited a more homogeneous phase distribution with a significantly reduced air void content, suggesting that the alkali-activated binder led to enhanced matrix densification and lower porosity. This densification in the HC-AA sample may be attributed to chemical interactions between hemp and the alkaline activator. Previous studies have reported that alkaline solutions, such as NaOH, can induce chemical delignification in plant-based materials, leading to lignin extraction and partial decomposition of the organic components [39]. Since hemp shivs share compositional similarities with wood, exposure to NaOH solution and water glass, as used in this study, could have altered their surface morphology and structural integrity [14]. Consequently, the hemp shivs in HC-AA may have become smaller, more compactable, or structurally weakened, making them more susceptible to compression during the compacting process, ultimately leading to the denser microstructure observed in **Fig. 6**.

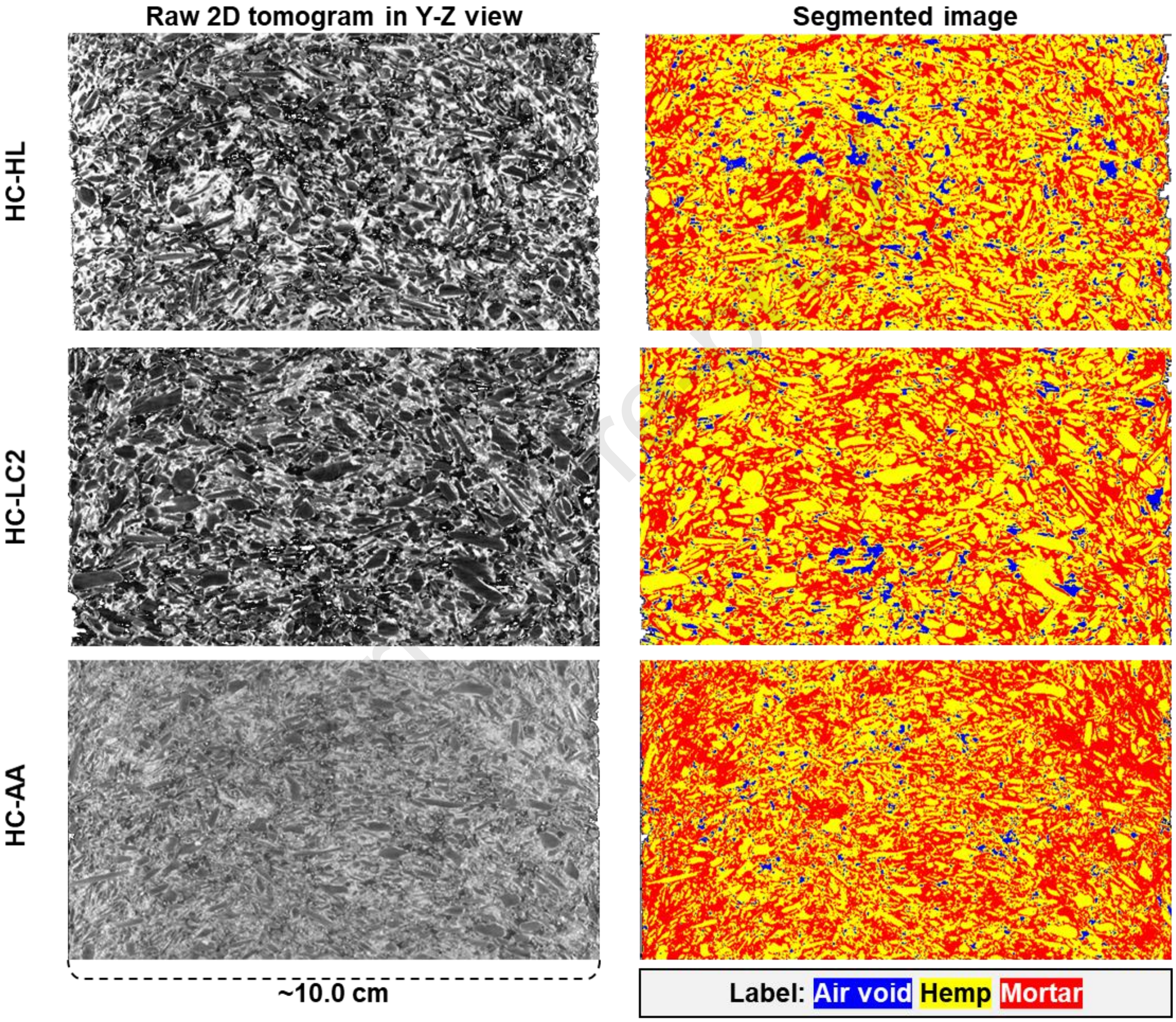

Fig. 6. Raw and segmented 2D tomograms of hempcrete samples using Aviso software.

Fig. 7 presents the volume fractions of the three phases (air void, hemp shivs, and mortar) identified through CT analysis, as depicted in **Fig. 6**. In this study, all hempcrete samples were fabricated under the same compaction degree, curing conditions, and mixing ratios, except for the precursor and mixing solution composition. However, the volumetric distribution of air voids, hemp shivs, and mortar significantly varied within the hempcrete.

The HC-AA sample exhibited the highest fraction of the mortar phase (53.9%) and the lowest fractions of air voids (2.7%) and hemp shivs (43.4%), whereas the HC-HL and HC-LC2 samples had relatively lower mortar content and higher air void and hemp fractions. The reduction in air void and hemp volume in the HC-AA sample suggests that the alkali-activated binder led to improved densification of the matrix. This aligns with the **Fig. 4** findings, which indicate that HC-AA had the highest air-dried bulk density among the three samples.

Given that all samples underwent the same compaction procedure, the differences in volume fractions imply that the fresh paste workability and hemp distribution were influenced by the binder type. The relatively higher inclusion of the denser mortar phase in HC-AA could be attributed to its enhanced packing efficiency and binder-hemp interaction during the mixing and casting process. Additionally, the reduced air void fraction in HC-AA suggests a more consistent matrix, which may be due to the interaction between the alkaline activator and the hemp surface, potentially altering the surface morphology of the hemp shivs. This phenomenon requires further investigation to determine whether the alkaline conditions affected the hemp shiv structure and contributed to the increased matrix density.

Furthermore, HC-HL and HC-LC2 exhibited more pronounced air voids and less compacted mortar, which could explain their lower density and mechanical strength compared to HC-AA. This emphasises the role of binder selection in optimising hempcrete's microstructural characteristics and overall performance.

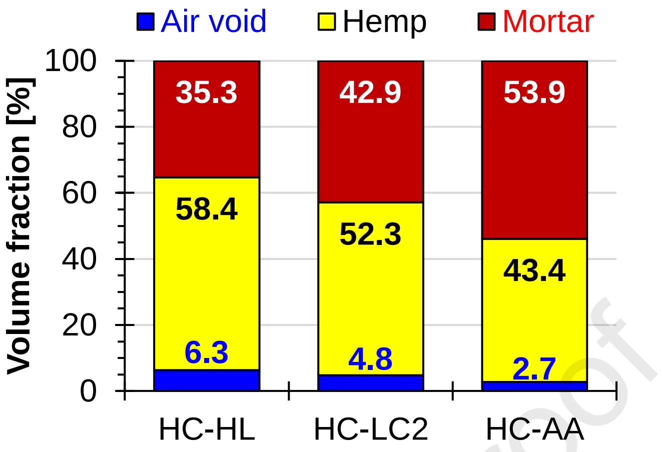

Fig. 7. Volume fractions of air void, hemp, and mortar phases in hempcrete samples.

3.2.2. Label Analysis on Hemp Phase

Fig. 8 illustrates the detailed label analysis process applied to the hemp phase in HC-HL. This analysis focused on segmenting individual hemp shivs from the bulk hemp phase, which was initially recognised as a single connected phase. To achieve this, the label analysis function in Avizo was utilised to identify and separate individual hemp shivs.

As shown in **Fig. 8** (a), an erosion process was applied to refine the segmentation of the hemp phase. Initially, without sufficient erosion, the hemp phase remained as a single bulk mass, preventing proper separation of individual shivs. By gradually increasing the erosion factor (1, 3, and 5 pixels), the segmentation improved, leading to a better distinction between individual hemp phases. However, excessive erosion could lead to over-segmentation or the loss of finer hemp structures, indicating that an optimal erosion factor is required to achieve accurate segmentation.

As shown in **Fig. 8** (b), despite the erosion process with the factor at 5 pixels, some hemp phases remained as bundled clusters of interconnected segments that were not clearly segmented. To separate these clusters into individual hemp shivs, further label analysis in Aviso software was performed after one more erosion process with the factor at 2 pixels. Afterwards, hemp phases were well-labelled, but certain hemp fragments still remained incorrectly segmented [see the red dashed line in **Fig. 8** (b)]. These incorrectly segmented hemp phases had unrealistically small widths, lengths, or volumes, which differed significantly from the typical hemp shiv dimensions (see **Fig. 2**). These misidentified phases were excluded from the final analysis to ensure data reliability, as they were considered too small to represent the actual hemp shiv size.

This process emphasises the importance of proper segmentation techniques in μCT analysis, as well as the need for careful parameter selection when using image-processing software like Avizo. The findings suggest that erosion plays a critical role in separating individual hemp shivs, and an appropriate filtering criterion is necessary to exclude erroneous data points.

Recent advances in μCT-based fibre analysis, such as the destruction-filtering-repairing (DFR) method proposed by Yang et al. [40], have shown that iterative segmentation can achieve near-pixel-level accuracy in extracting fine fibres from heterogeneous matrices, thereby improving the reliability of orientation estimation. While the present study used threshold-based segmentation combined with erosion and labelling steps in Avizo, such advanced iterative filtering methods could be used in future studies to more effectively separate hemp hurds from binders and improve the quantification of 3D orientation indices (e.g., θ distribution).

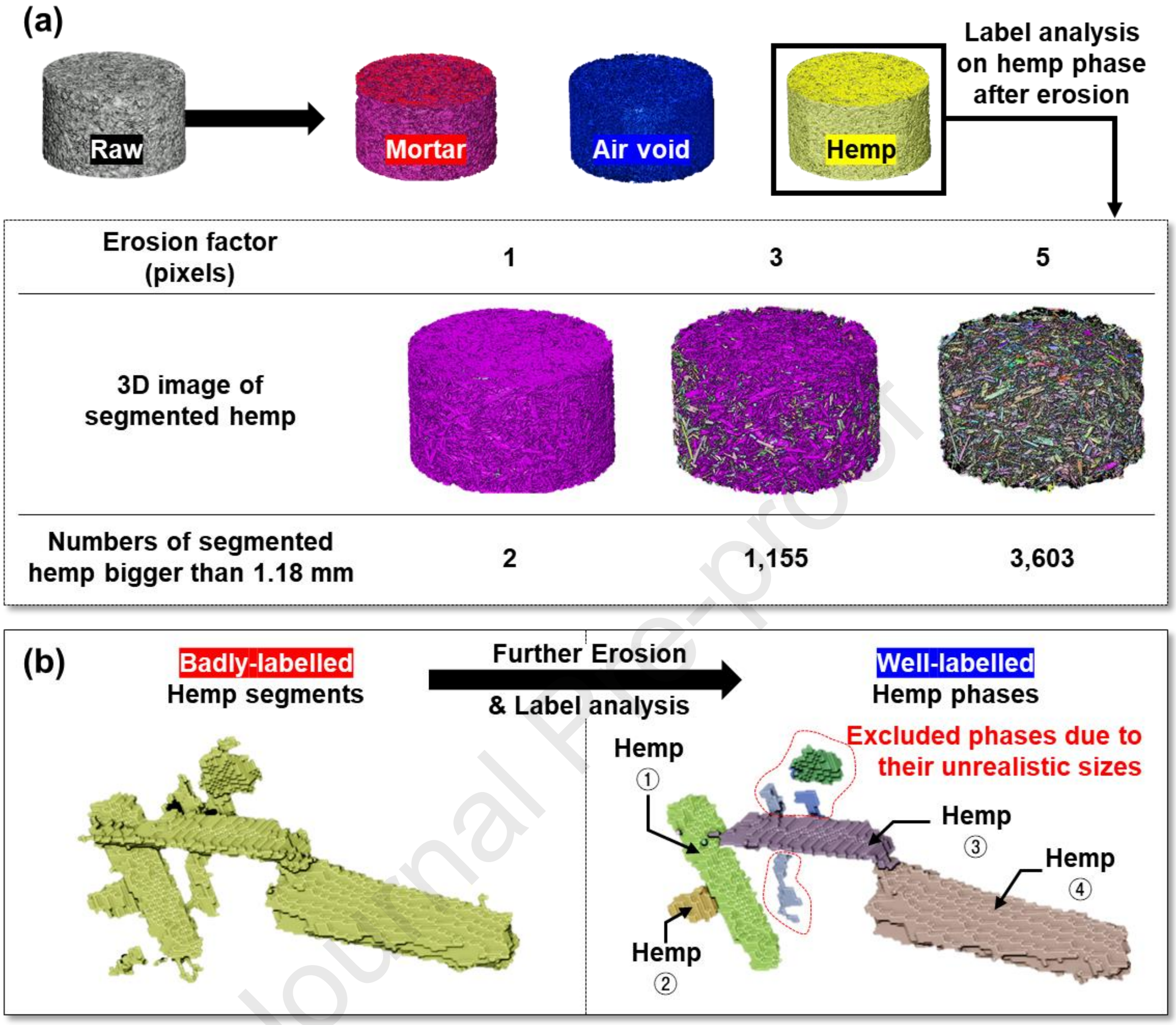

Fig. 8. Example of label analysis on hemp phase in HC-HL: (a) 3D images of hemp using different erosion factors at 1, 3, and 5 pixels and (b) further erosion and label analysis on badly-labelled hemp segments.

Using the properly labelled hemp shivs, the present study visualised their spatial alignment to understand their distribution and orientation in our hempcrete samples. **Fig. 9** illustrates the 3D visualisation of individually labelled hemp shivs in the spherical coordinate system. Here, radial distance (r), inclination angle (θ; denoting the angle between the shiv orientation vector and the Z-axis), and azimuthal angle (φ) denote the angle of rotation of the radial line around the polar axis. This analysis was conducted using the labelled hemp data extracted from the segmentation process in Avizo, where various geometric and positional parameters of each hemp shiv were obtained, including width, length, spatial coordinates (X, Y, Z), θ, and principal orientation vector components.

To represent the shiv orientation, a 3D cylindrical model was used to visualise each hemp shiv in MATLAB. To ensure that shivs pointing upward and downward were treated equivalently, the absolute value of the Z-component of the orientation vector was used. As a result, the θ range is represented in blue to red, from 0° (completely vertical) to 90° (completely horizontal). This approach allowed for a clear differentiation of shiv alignment within the hempcrete matrix.

For consistency and to enhance visibility, only a subset of hemp shivs was selected for this analysis. Specifically, shivs with a width and length larger than 1.18 mm were chosen, as this size range represented the most frequently occurring hemp size observed in **Fig. 2**. The criteria for the subset were derived from the raw hemp shivs and thus the subset used in the analysis would reasonably represent the overall distribution and orientation of hemp shivs for the qualitative comparison of different hempcretes.

However, it is important to note the limitations of the erosion-based segmentation method. The erosion factor influences the number and shape of segmented hemp shivs, as it removes surface pixels to separate interconnected hemp phases. This process might result in partial loss of hemp boundaries, meaning that the segmented hemp shiv shapes may not fully represent the true dimensions of the original shivs. Nevertheless, this approach proved effective for comparative analysis of hemp orientation and quantity among hempcrete samples incorporating different binder types, which was the primary objective of this study.

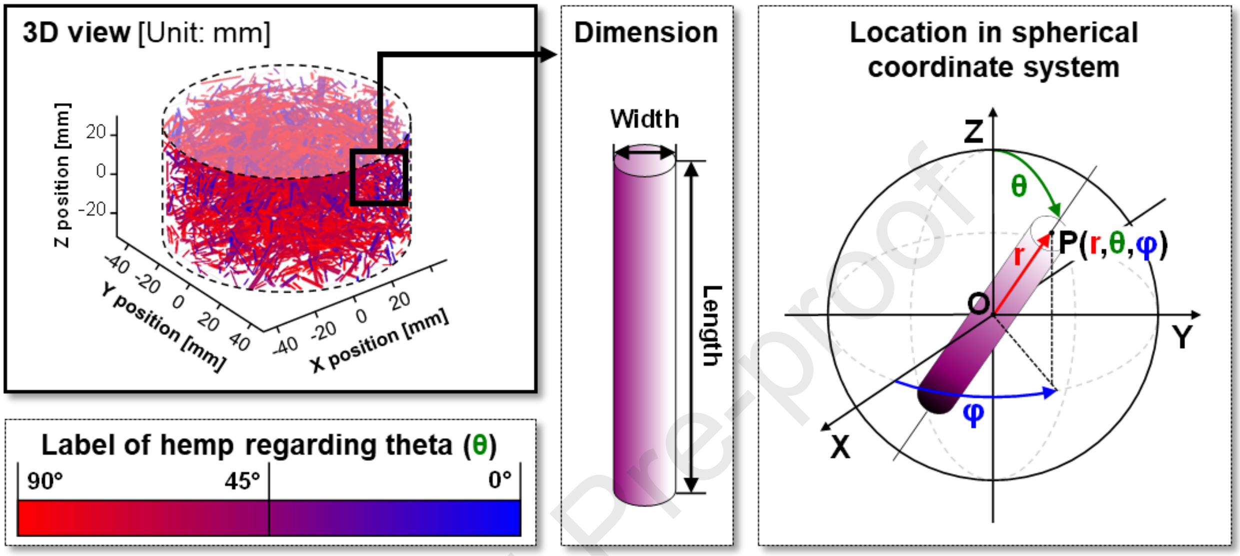

Fig. 9. 3D full view of the specified hemp labelled in theta value. These hemp pieces represent hemp shivs contained in subsections classified by (i) length, (ii) width, and (iii) length/width ratio among the segmented hemp phases contained in the HC-HL sample.

Fig. 10 illustrates the 3D view, plan view, and elevation view of segmented hemp shivs within different hempcrete samples. The spatial distribution and orientation of the shivs are critical factors influencing the mechanical and thermal performance of hempcrete [41]. All samples showed that hemp shivs appeared to be more randomly oriented, but the HC-AA sample exhibited a significantly lower number of hemp shiv phases compared to other samples. This observation is consistent with the volumetric data presented in **Fig. 7**, which showed that HC-AA contained the lowest volume fraction of hemp among the samples. However, it should be noted that, although the same content of hemp was added to all samples during mixing (see **Table 2**), the HC-AA sample exhibited a noticeably lower number of segmented hemp shivs in the image analysis. This difference is further discussed in the following Section 4.2, where the influence of chemical treatment (e.g., delignification under alkaline activation) and potential segmentation limitations due to grayscale image contrast are considered. These factors may have altered the visibility and morphology of hemp phases, resulting in reduced detectability during μCT image processing.

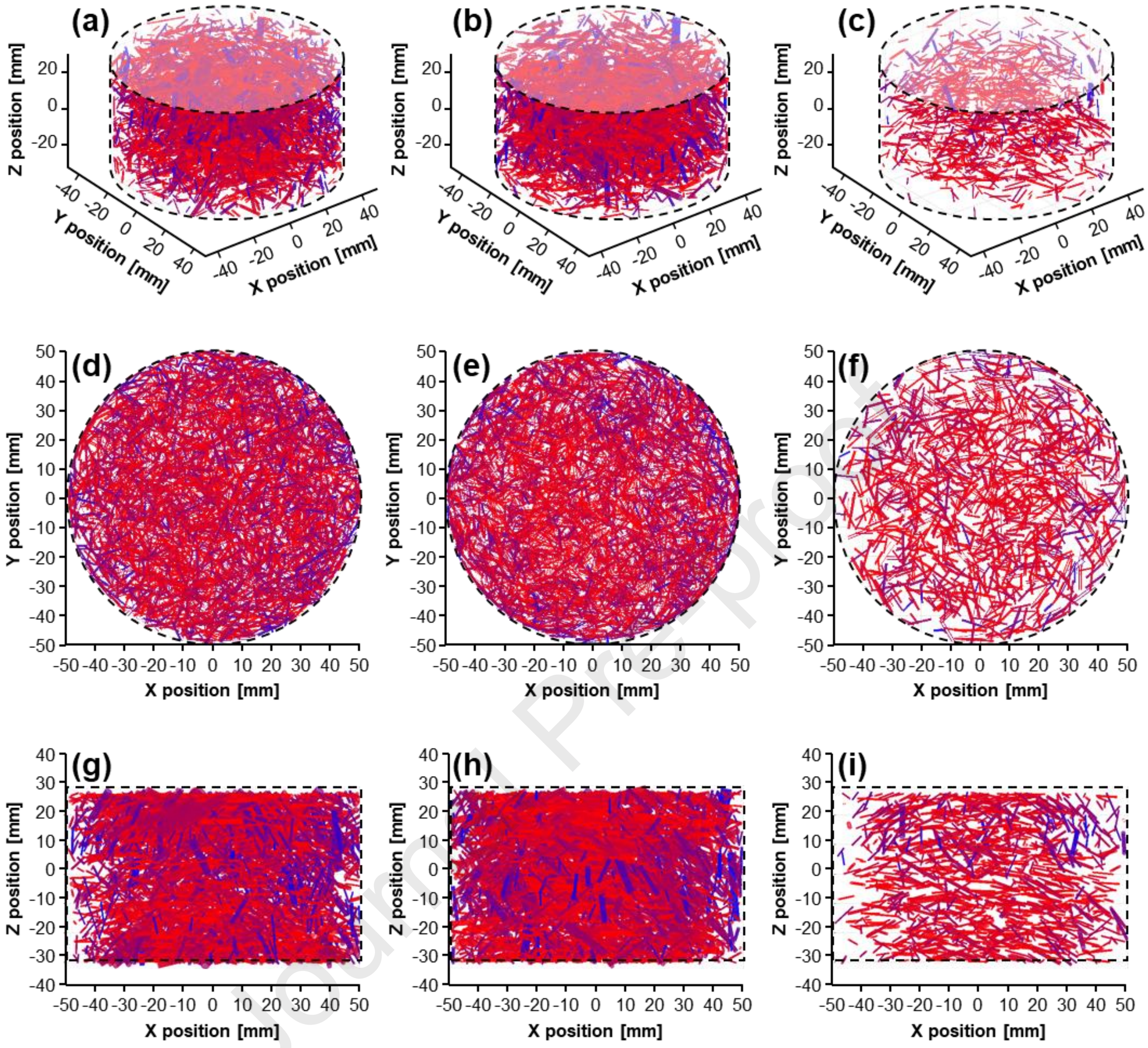

Fig. 10. (a–c) 3D view, (d–f) plan view, and (g–i) elevation view of segmented hemp shivs in HC-HL [see (a), (d), and (g)], HC-LC2 [see (b), (e), and (h)], and HC-AA [see (c), (f), and (i)] samples. The inclination angle of hemp is presented in blue to red, indicating vertical to horizontal.

Fig. 11 shows the orientation and dimensional distribution of hemp shivs in the three hempcrete samples. As illustrated in **Fig. 11** (a), all samples exhibited predominantly horizontal alignment, with the highest degree of alignment above 45°, which may reduce vertical pore connectivity and heat transfer. Moreover, HC-AA showed higher numbers of hemp shivs with a degree of alignment above 75°, compared to other samples. The orientation of hemp shivs might affect thermal transport behaviour in hempcrete due to their internal porous structure [41]. As hemp shivs are bio-derived, their vascular pores are typically elongated along the stem axis [30], promoting anisotropic heat transfer [42]. When shivs are aligned horizontally (i.e., perpendicular to the direction of heat flow), these pores can interrupt vertical heat conduction, thereby enhancing the insulating performance of the composite.

In **Fig. 11** (b) and (c), all samples showed similar ranges of hemp shiv width (1.5–2.5 mm) and length (4–8 mm). However, HC-AA exhibited a greater proportion of smaller shivs than the other samples. For example, the normalised distribution of width in the 1.0–2.5 mm range was 92.0% in HC-AA, compared to 86.7% in HC-HL and 82.9% in HC-LC2. Meanwhile, the proportion of hemp shiv lengths between 2–8 mm was 78.0% in HC-AA, which was similar to HC-HL (81.5%) and HC-LC2 (78.3%). This confirms that HC-AA contained finer hemp shivs, which may influence both the mechanical interlock and thermal conductivity of the composite.

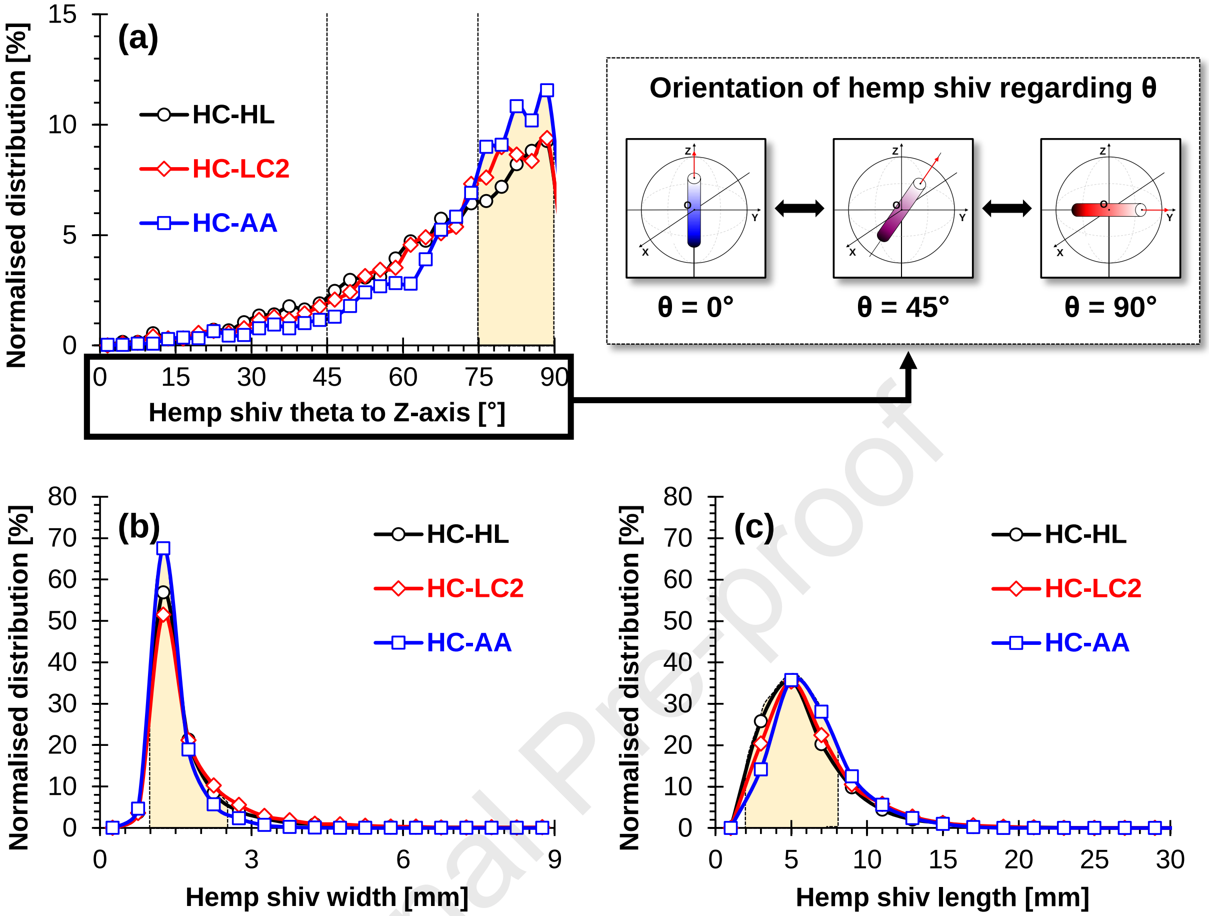

Fig. 11. Normalised distribution of hemp shivs regarding their (a) theta to Z-axis, (b) width and (c) length.

4. Discussions

4.1 Binder Effect on Physical and Mechanical Properties of Hempcrete

The density and compressive strength of hempcrete were significantly influenced by the binder type. HC-AA exhibited the highest bulk density, adhesion, and compressive strength [see **Fig. 4** (a–c)].

Fig. 12 correlates the physical and mechanical properties of hempcrete samples and their volume fractions (φ) of the three phases identified in μCT (air void, hemp, and mortar in **Fig. 7**). The correlation coefficient (r) value indicates the degree of linear relationship between the two variables. Moreover, it should be noted that because only limited data were used in this study, the regression lines are presented only to illustrate the general trends observed from the experimental results and do not imply any statistical significance."

The trends in **Fig. 12** consistently show that higher mortar fractions are positively correlated with density, strength, and adhesion, while higher hemp and air void ratios lead to negative correlations. These trends were observed for all three measured properties, suggesting a common underlying mechanism between phase composition and hempcrete performance.

The correlation for the physical and mechanical properties of all phases in μCT showed a strong linear relationship, with absolute r values ranging from about 0.96 to 0.99. Hemp and air voids have lower specific gravity than mortar, and so their increasing content leads to a lower density [30]. Furthermore, they are weaker than mortar, and their increasing content also leads to the degradation of mechanical properties such as adhesion and compressive strength. Then, higher air void and hemp fractions resulted in lower density and strength, consistent with the relationship between porosity and mechanical properties. Likewise, a higher mortar fraction was positively correlated with compressive strength ($r = 0.97$), reinforcing the role of a denser binder matrix in improving mechanical integrity. Thus, these demonstrate that the binder-to-hemp ratio can be optimised to meet the structural limit of hempcrete as a building material.

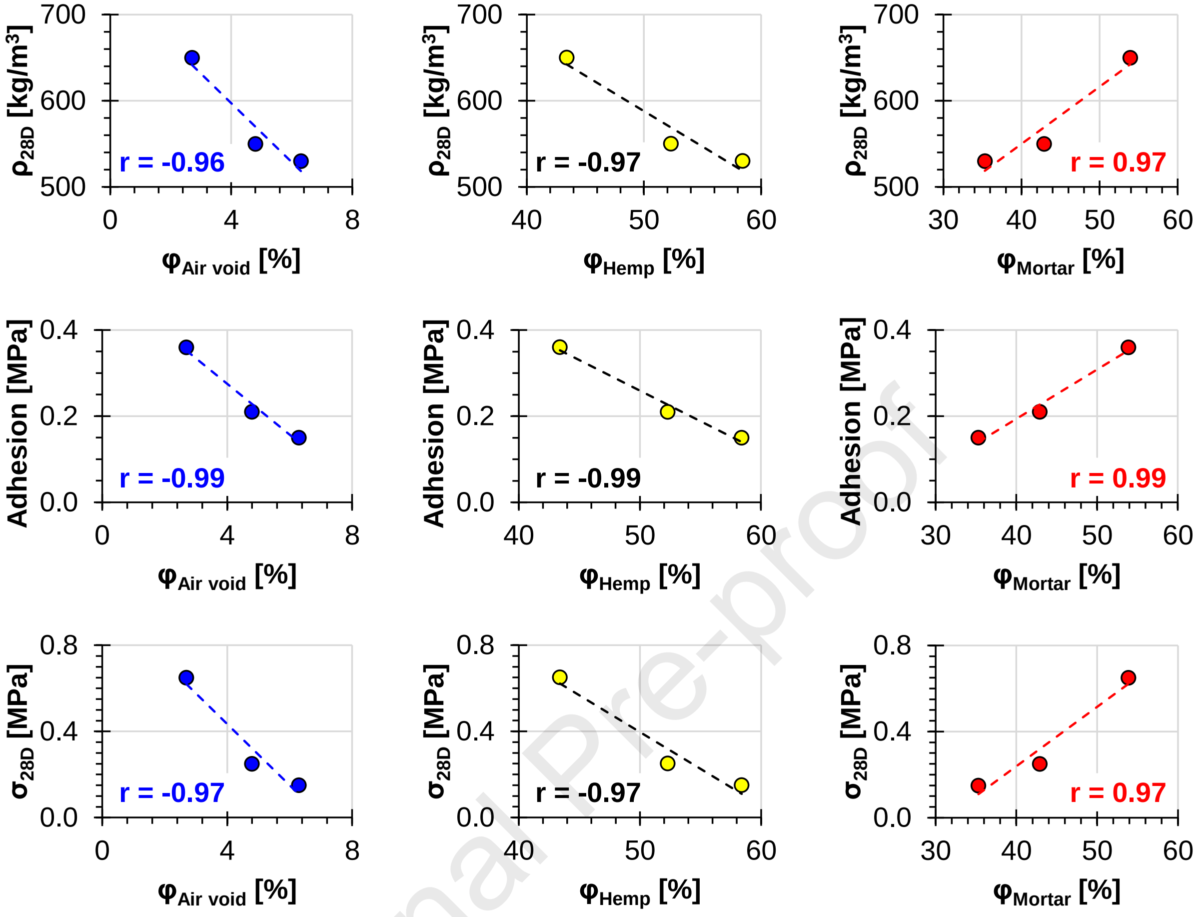

Fig. 12. Linear relationship of the volume fractions (φ) of air void, hemp, and mortar phases in μCT with 28-day bulk density (ρ_{28D}), adhesion, and 28-day compressive strength (σ_{28D}) of hempcrete samples.

4.2. Binder Effect on Thermal Property of Hempcrete

Fig. 13 illustrates the correlations between the thermal conductivity (λ_{28D}) of hempcrete samples and the volume fractions (φ) of the three phases in μCT (air void, hemp, and mortar in **Fig. 7**). The regression analysis also revealed a strong linear correlation because the absolute r value was around 0.97 to 0.98. However, it should be noted that counter-intuitive trends were observed in thermal conductivity properties and the volume fraction of the three phases in hempcrete. For example, the HC-AA sample exhibited the highest bulk density, adhesion, and compressive strength [see **Fig. 4** (a–c)] among all binder types, but had the lowest thermal conductivity [see **Fig. 4** (d)]. Notably, similar findings have also been reported in the previous study [13].

The observation that HC-AA combines the highest compressive strength and lowest thermal conductivity (**Fig. 4**) is counterintuitive to the conventional density-conductivity relationship. Similarly, the trends in **Fig. 13** cannot be explained solely by phase fraction. However, these results can be better interpreted using the μCT analysis, which revealed other governing microstructural factors such as phase connectivity, particle orientation, and binder-hemp interfacial properties. The three-dimensional structural insight provided by μCT demonstrates that heat transfer in hempcrete depends not only on the amount of each phase but also on its spatial arrangement and connectivity, which provides a justification for HC-AA experimental results.

Although this counter-intuitive result suggested the superior mechanical and thermal performance of alkali-activated binder for hempcrete applications, this result requires further explanation. Typically, an increase in solid fraction enhances heat transfer due to greater cross-sectional contact between particles, whereas higher air void content reduces conductivity due to the insulating effect of air. Therefore, this unexpected result suggests that thermal behaviour in hempcrete is governed not solely by bulk-phase thermal conductivity but also by microstructural factors.

This hypothesis is further supported by the lack of correlation between the thermal conductivities of mortars and their corresponding hempcrete composites (see **Fig. C1**). If binder thermal conductivity were the dominant factor, one would expect both values to follow similar trends. However, in this case, the HC-AA sample, with high thermally conductive mortar, resulted in the lowest composite thermal conductivity [see **Fig. 4 (d)**]. μCT-based volumetric analysis revealed that the HC-AA sample had the lowest volume fractions of both air voids and hemp shivs, but the highest volume fraction of mortar (see **Fig. 7**). In other words, a higher amount of mortar alone does not guarantee improved thermal transfer. Instead, the limited presence of insulating hemp and disconnected or non-continuous mortar regions, possibly due to weak interaction at the interface or disrupted thermal pathways, may have restricted heat conduction within the composite.

Thus, to understand the underlying mechanisms, the present study employed μCT analysis to evaluate 3D microstructural properties such as (i) matrix density, (ii) the total number of hemp shivs after the labelling analysis, (iii) orientation, and (iv) dimension of hemp shivs (see **Fig. 10** and **Fig. 11**).

HC-AA exhibited a denser internal matrix compared to the other samples (see **Fig. 5**, **Fig. 6**, and **Fig. 7**). Based on the mix proportions (see **Table 2**) and the specific density (see **Table 1**) of each binder component, the estimated density for blended precursors in AA binder can be calculated as 2.60 g/cm^3 [i.e., (21.7·2.55+9.3·2.72)/31.0]. Likewise, these density values in HL and LC2 binders were 3.02 and 2.78 g/cm^3, respectively. This indicates that, under identical mass-based additions, AA binder occupies a greater volume, which aligns with the volume fraction results obtained from μCT (see **Fig. 5**, **Fig. 6**, and **Fig. 7**). After 28 days, the bulk density also followed this volumetric trend [see **Fig. 4 (a)**]. Furthermore, due to differences in binder reactivity, the rate of moisture loss varied among samples. HC-AA, having the lowest binder density, showed the highest weight loss (15.2%), while HC-HL and HC-LC2 weight losses were only 10.4% and 9.9%, respectively. This suggests that the AA mortar not only filled more space initially but also formed additional micro-voids through water evaporation during curing due to its faster drying than other samples. These newly formed pores within the mortar matrix likely contributed to the lower thermal conductivity observed in the HC-AA sample.

From the μCT analysis [see **Fig. 10** (c,f, and i)], the total hemp count in HC-AA was notably lower than in other hempcrete samples. While all samples were prepared with identical weights of hemp, binder, and mixing solution (see **Table 2**), the volume fractions of hemp, mortar, and air voids notably varied (see **Fig. 6** and **Fig. 7**). This indicates further compaction and possible reduction of the volume of hemp shivs in HC-AA, which may remove the hemp during the labelling analysis. The volume fractions of subsected hemp among the total labelled hemp phases, compared by the number of voxels in μCT, were 80.1, 87.7, and 64.5% for HC-HL, HC-LC3, and HC-AA, respectively. Since the weight fraction of hemp >1.18 mm was around 89.5% (see **Fig. 2**), HC-AA was compressed more easily than the other samples, even though all samples were subjected to the same degree of compression. It should be noted that only hemp is highly compressible, while other components (precursors, sand, and mixing solution in **Table 2**) are incompressible under the compaction force applied during the hempcrete fabrication. This increased compactness of hemp might be attributed to the physicochemical effects of the alkaline activator. Chemically, NaOH and sodium silicate might have softened the hemp surface through the delignification process [6, 43, 44], making it more compressible. Physically, the high viscosity of the alkaline activator [45] likely limited its penetration into the hemp [46, 47], leaving internal pores unfilled and the shivs more prone to flattening under tamping pressure. Consequently, HC-AA samples exhibited reduced apparent hemp volume in μCT analysis, despite identical initial mix proportions.

Third, the distribution of horizontally aligned hemp shivs was less prominent in HC-AA, which may have influenced heat transfer behaviour, given that the Hot Disk thermal analyser applies heat from the top surface. This implies that hemp shiv orientation and connectivity in HC-AA may have disrupted vertical thermal conduction paths, despite the larger volume of the matrix.

Fourth, the hemp shivs of HC-AA became finer than other samples through alkaline activation using NaOH and water glass. Therefore, the internal pore structure of the hemp pieces may cause shrinkage, which may affect the heat transfer and tortuosity of the heat path, because the thermal conductivity increases when the cross-sectional area of the solid increases or the tortuosity of the heat transfer path decreases [48, 49]. Moreover, Haemin et al. [30] observed that NaOH-treated (i.e., delignified) hemp exhibited increased pore size and reduced overall porosity, leading to lower thermal conductivity in hempcrete. Given that the HC-AA mixture in this study used NaOH and sodium silicate as activators, these alkaline components might have modified the pore structure of the hemp shivs or the surrounding matrix, further contributing to reduced heat transfer.

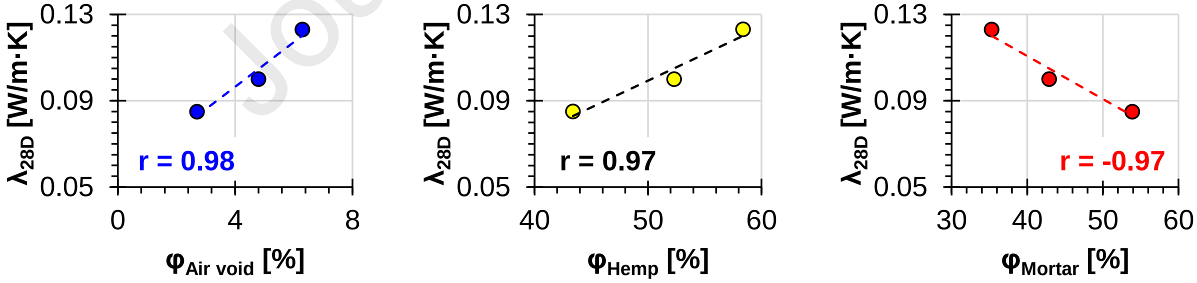

Fig. 13. Linear relationship of the volume fractions (φ) of air void, hemp, and mortar phases in µCT with 28-day thermal conductivity (λ_{28D}) of hempcrete samples.

4. Conclusions

This study employed μCT analysis to newly investigate the influence of the 3D properties of hemp shivs (dimensions, orientation, and distribution) on the hempcrete performance with low-carbon binders. Limestone calcined clay (LC2) and alkali-activated (AA) binders were evaluated in comparison to a reference hydrated lime (HL) binder. These detailed findings will provide new microstructural understandings to support the sustainable hempcrete design. The detailed findings are as follows:

- Despite the inherently low compressive strength of hempcrete (<1 MPa), the HC-AA samples exhibited ~ 4.1 times higher strength than the reference binder hempcrete (HC-HL), whereas the increase in compressive strength was only about 60% for the limestone calcined clay hempcrete specimens.
- The HC-AA sample also showed the lowest thermal conductivity: 15.0–30.9% lower than those of HC-LC2 and HC-HL, respectively. Interestingly, the thermal conductivity of hempcrete did not primarily correlate with that of its corresponding mortar, suggesting that bulk-phase conductivity alone does not govern thermal performance. Instead, complicated microstructural interactions appear to be significant.
- Among the binders in this study, the alkaline-activated binder provided the best compressive strength and thermal insulation in hempcrete.
- To understand the underlying mechanism of this result, μCT analysis was conducted to identify the microstructural factors of hempcrete. The HC-AA sample had the highest matrix density due to a greater volume of mortar (53.9%) compared to other binders (35.3–42.9%). Moreover, the alkaline-activated binder induced more horizontally aligned hemp shivs and generated smaller hemp shivs, likely due to chemical modification under alkaline conditions.

- Notably, the enhanced thermal performance of HC-AA is due to not only the phase composition alone, but also the interactions between the three phases (pores, hemp, and mortar), and microstructural factors, particularly matrix density and hemp orientation and shiv size. In particular, a counterintuitive correlation was observed whereby thermal conductivity increased with increasing air void or hemp content. Using μCT, this behaviour was linked to the pore structure and hemp-binder interfacial characteristics, providing new insights into the microstructure-property relationships of hempcrete.

Acknowledgement

This research was funded by the Australian Hemp Masonry Company Pty. Ltd. and the ARC Linkage project LP200200779 titled “Decarbonising built environments with hempcrete and green wall technology”.

Declaration of Competing Interest

The authors declare that they have no known competing financial interests or personal relationships that could have appeared to influence the work reported in this paper.

Appendix A. Particle Size Distribution and Mineral Composition of Raw Precursors

Fig. A1 shows the particle size distribution of the raw precursors measured by using a particle size analyser, and **Fig. A2** illustrates their mineral composition scanned by using an X-ray diffractometer.

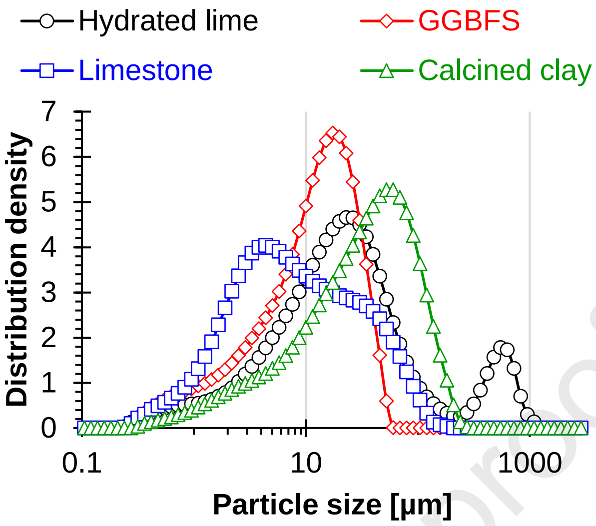

Fig. A1. Particle size distribution of raw precursors.

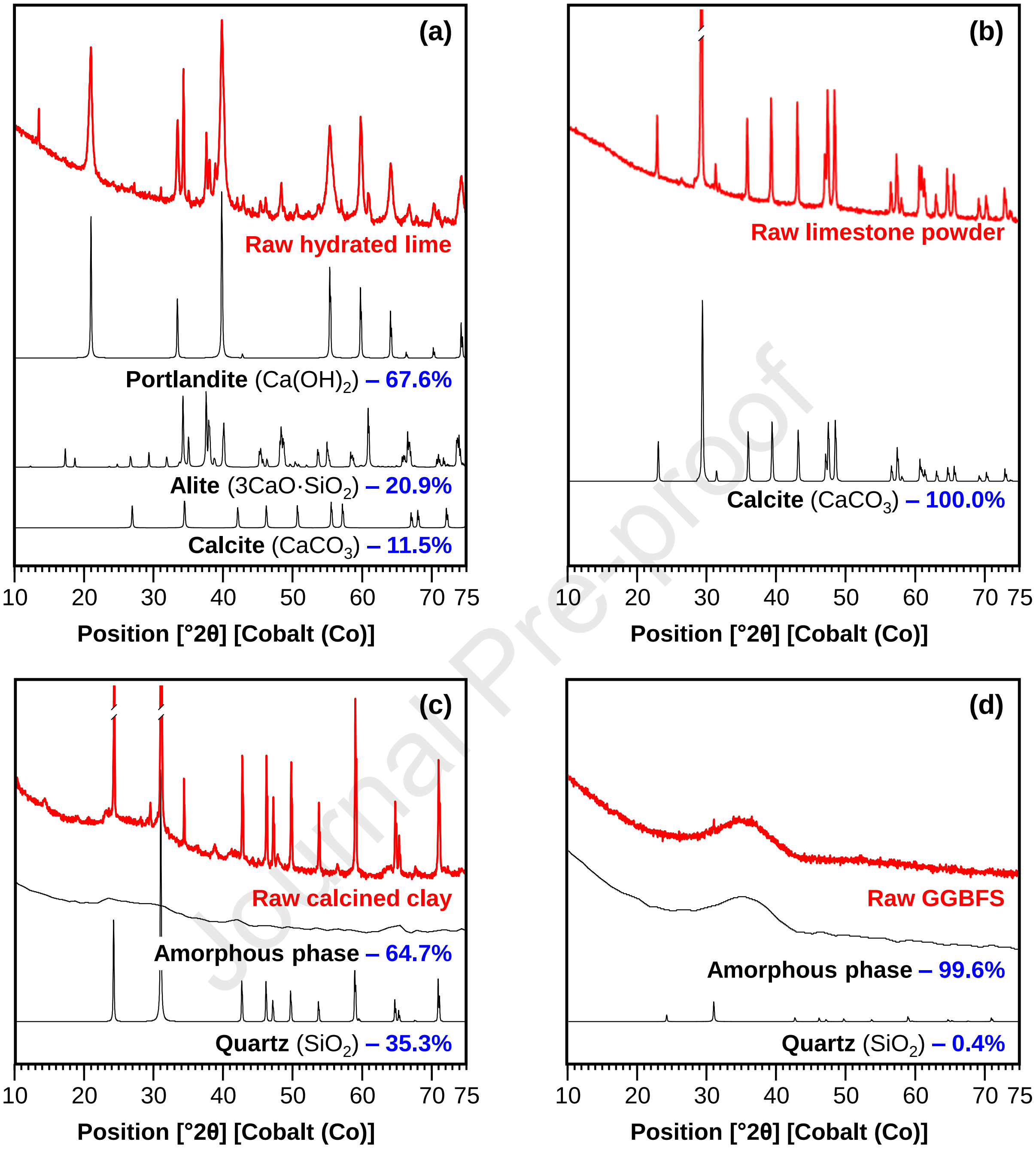

Fig. A2. Mineral compositions of raw precursors.

Appendix B. Water Absorption of Hemp Shivs

Fig. B1 illustrates the water absorption of hemp shivs. According to the RILEM TC 236 [50], the initial water content (INC) of hemp shivs was assessed to calculate the water content to make hemp shivs in a saturated surface dried condition. The water absorption of three hemp specimens was measured from 1 minute to 48 hours. The water content at a specific time, W(t), can be computed as shown in **Eq. 1**. Here, m(t) denotes the hemp mass at the time (t) after immersion, while m_d denotes the oven-dried hemp mass.

$$W(t) = (m(t) - m_d)/m_d \times 100 \quad (1)$$

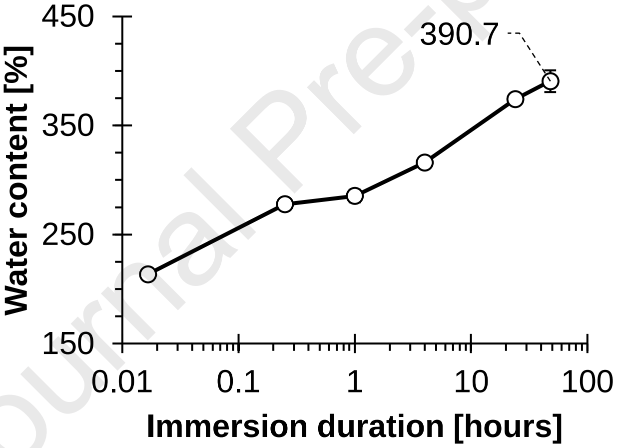

Fig. B1. Water absorption of hemp shivs.

Appendix C. Thermal Conductivity of Mortar and Hempcrete Samples

Fig. C1 compares the thermal conductivity of mortar and hempcrete samples, which were measured as denoted in the previous section 2.3.2.1. Thermal conductivity measurements were conducted for both mortars and hempcrete composites formulated with the three different binders considered in this study. While the thermal conductivity of the hempcrete varied notably depending on the type of binder, the mortar samples varied only marginally with the type of binder used. This observation suggests that, in hempcrete composites, the binder type is not the dominant factor affecting thermal conductivity. Instead, the influence of the hemp shiv might be more significant in governing the thermal properties of hempcrete.

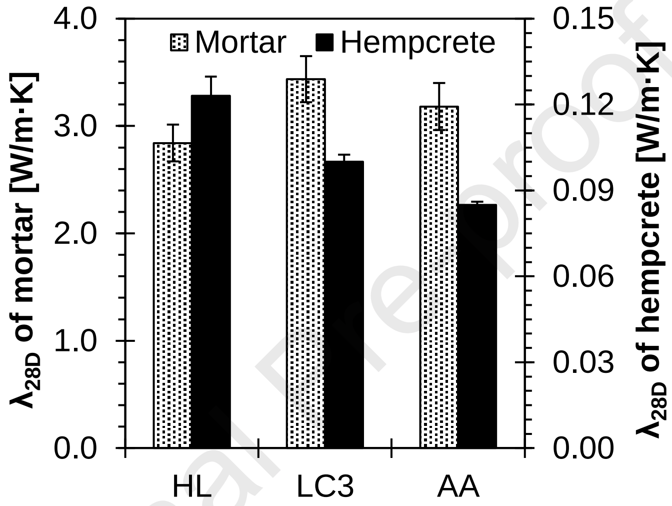

Fig. C1. Comparison of the 28-day thermal conductivity of mortar and hempcrete samples.

Appendix D. Statistical Analysis on Hempcrete Properties

As shown in **Table D1**, differences in 28-day bulk density, 28-day adhesion, 28-day compressive strength, and 28-day thermal conductivity data of the different hempcrete samples were compared using one-way analysis of variance (ANOVA), followed by pairwise comparisons with Tukey's honestly significant difference (HSD) test. ANOVA results confirmed that bulk density exhibited statistically significant differences among all binder types (F = 2,578.67, $p < 0.001$), further supported by Tukey's test, where all pairwise comparisons yielded p-values < 0.001.

Similarly, adhesion showed significant group differences (F = 9.73, p = 0.013), with HC-AA exhibiting significantly higher adhesion than HC-HL (p = 0.013) and HC-LC2 (p = 0.046). For compressive strength (F = 14.97, p = 0.005), HC-AA showed significantly greater strength than both HC-HL (p = 0.005) and HC-LC2 (p = 0.014), while the difference between HC-HL and HC-LC2 was not significant (p = 0.591). Lastly, thermal conductivity also revealed clear distinctions among all groups (F = 150.33, p < 0.001), with all pairwise comparisons showing highly significant differences (p < 0.001), where HC-AA had the lowest and HC-HL the highest conductivity values, consistent with **Fig. 4**.

Table D1. ANOVA and Tukey's HSD test results for hempcrete properties.

Metric	ANOVA		Tukey's HSD test		
	F-statistic	P-value	Group 1	Group 2	P-value
28-day bulk density	2,578.67	<0.001	HC-AA	HC-HL	<0.001
			HC-AA	HC-LC2	<0.001
			HC-HL	HC-LC2	<0.001
28-day adhesion	9.73	0.013	HC-AA	HC-HL	0.013
			HC-AA	HC-LC2	0.046
			HC-HL	HC-LC2	0.538
28-day compressive strength	14.97	0.005	HC-AA	HC-HL	0.005
			HC-AA	HC-LC2	0.014
			HC-HL	HC-LC2	0.591
28-day thermal conductivity	150.33	<0.001	HC-AA	HC-HL	<0.001
			HC-AA	HC-LC2	<0.001
			HC-HL	HC-LC2	<0.001

Appendix E. Visual Appearance of Hempcrete Samples.

Fig. E1 presents the visual appearance of hempcrete samples prepared with the three different binders. They exhibited distinct colour variations, reflecting the different compositions of the binders (see **Fig. 1**). HC-HL appeared the lightest in colour, primarily due to the high content of hydrated lime, whereas HC-LC2 had a slightly darker tone due to the presence of calcined clay. In contrast, HC-AA exhibited a noticeably brownish hue, attributed to the combination of calcined clay and GGBFS.

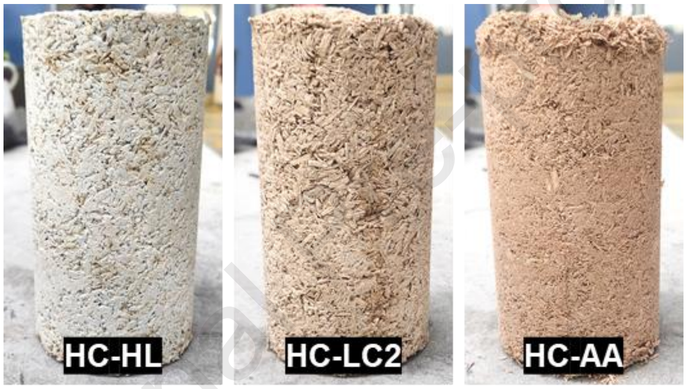

Fig. E1. Hempcrete samples with three different binders.

References

[1] International Energy Agency, World Energy Outlook 2021, International Energy Agency, Paris, France, 2021, p. 383.

[2] Z. Ma, Y. Wu, K. Fang, Y. Zhang, C. Wang, Developing fully recycled alkali-activated mortar made with waste concrete fines as a substitute for both binder and sand: Multi-properties evaluation, Construction and Building Materials 477 (2025) 141323.

[3] Z. Yao, R. Pal, H. Song, A. Van de Keere, A. Kashani, E. Gruyaert, T. Kim, Chloride transport, binding, and microstructure in alkali-activated concrete with different types of precursor combinations, Cement and Concrete Research 198 (2025) 108002.

[4] C. Wang, J. Guo, X. Wang, Y. Zhang, Z. Ma, Dynamic mechanical properties and damage constitutive model of high-toughness recycled aggregate concrete under high strain rate impact loads, Journal of Building Engineering 106 (2025) 112589.

[5] C. Wang, Y. Lu, Y. Dai, H. Wu, Z. Ma, In-situ 4D CT analysis of microcrack evolution in carbonated fiber-reinforced recycled aggregate concrete, Cement and Concrete Composites (2025) 106161.

[6] H. Song, D. Kim, S. Yoon, W.S. Yum, D. Jeon, J.E. Oh, Development of artificial leak-free phase change material (PCM) aggregates using emulsion technique, cementless binder, and cold-bonded pelletization, Construction and Building Materials 411 (2024) 134293.

[7] H. Song, S. Yoon, J.E. Oh, J.-I. Suh, Thermal performance evaluation of silica dip-coated phase change material beads for thermal energy storage in cement-based composites, Construction and Building Materials 425 (2024) 135907.

[8] S. Pretot, F. Collet, C. Garnier, Life cycle assessment of a hemp concrete wall: Impact of thickness and coating, Building and Environment 72 (2014) 223-231.

[9] D. Lelievre, T. Colinart, P. Glouannec, Hygrothermal behavior of bio-based building materials including hysteresis effects: Experimental and numerical analyses, Energy and Buildings 84 (2014) 617-627.

[10] P. Glé, E. Gourdon, L. Arnaud, Acoustical properties of materials made of vegetable particles with several scales of porosity, Applied Acoustics 72(5) (2011) 249-259.

[11] A. Arrigoni, R. Pelosato, P. Melià, G. Ruggieri, S. Sabbadini, G. Dotelli, Life cycle assessment of natural building materials: the role of carbonation, mixture components and transport in the environmental impacts of hempcrete blocks, Journal of Cleaner Production 149 (2017) 1051-1061.

[12] R. Walker, S. Pavia, Influence of the type of binder on the properties of lime-hemp concrete, Construction and Building Research, Springer, 2014, pp. 505-514.

[13] S.G. Nair, Q.D. Nguyen, Q. Zhu, M. Karimi, Y. Gan, X. Wang, A. Castel, P. Irga, C.G.d. Rocha, F. Torpy, Suitability of calcined clay and ground granulated blast furnace slag geopolymer binder for hempcrete applications, Built Environment Project and Asset Management (2025).

[14] M.P. Sáez-Pérez, M. Brümmer, J.A. Durán-Suárez, Effect of the state of conservation of the hemp used in geopolymer and hydraulic lime concretes, Construction and Building Materials 285 (2021) 122853.

[15] R. Walker, S. Pavia, R. Mitchell, Mechanical properties and durability of hemp-lime concretes, Construction and Building Materials 61 (2014) 340-348.

[16] T. Jami, S. Karade, L. Singh, A review of the properties of hemp concrete for green building applications, Journal of Cleaner Production 239 (2019) 117852.

[17] M.A. Jungclaus, S.L. Williams, J.H. Arehart, W.V. Srubar III, Whole-life carbon emissions of concrete mixtures considering maximum CO2 sequestration via carbonation, Resources, Conservation and Recycling 206 (2024) 107605.

[18] Z. Ebrahim, M. Mastali, M. Maguire, Toward sustainable lightweight durable bricks using alkali-activated hemp-based materials, Construction and Building Materials 369 (2023) 130609.

[19] F. Collet, S. Pretot, Thermal conductivity of hemp concretes: Variation with formulation, density and water content, Construction and building materials 65 (2014) 612-619.

[20] S. Elfordy, F. Lucas, F. Tancret, Y. Scudeller, L. Goudet, Mechanical and thermal properties of lime and hemp concrete ("hempcrete") manufactured by a projection process, Construction and Building Materials 22(10) (2008) 2116-2123.

[21] Q. Hu, M. Aboustait, T. Kim, M.T. Ley, J.C. Hanan, J. Bullard, R. Winarski, V. Rose, Direct three-dimensional observation of the microstructure and chemistry of C3S hydration, Cement and concrete research 88 (2016) 157-169.

[22] Q. Hu, M. Aboustait, T. Kim, M.T. Ley, J.W. Bullard, G. Scherer, J.C. Hanan, V. Rose, R. Winarski, J. Gelb, Direct measurements of 3d structure, chemistry and mass density during the induction period of C3s hydration, Cement and concrete research 89 (2016) 14-26.

[23] Z. Wu, Y. Wei, S. Wang, J. Chen, Application of X-ray micro-CT for quantifying degree of hydration of slag-blended cement paste, Journal of Materials in Civil Engineering 32(3) (2020) 04020008.

[24] J.-S. Kim, J.H. Kim, T.-S. Han, Microstructure characterization of cement paste from micro-CT and correlations with mechanical properties evaluated from virtual and real experiments, Materials Characterization 155 (2019) 109807.

[25] J. Schock, S. Liebl, K. Achterhold, F. Pfeiffer, Obtaining the spacing factor of microporous concrete using high-resolution Dual Energy X-ray Micro CT, Cement and Concrete Research 89 (2016) 200-205.

[26] M. Wevers, B. Nicolaï, P. Verboven, R. Swennen, S. Roels, E. Verstrynge, S. Lomov, G. Kerckhofs, B. Van Meerbeek, A.M. Mavridou, Applications of CT for non-destructive testing and materials characterization, Industrial X-ray computed tomography (2018) 267-331.

[27] I. Ceyte, Béton de chanvre, définition des caractéristiques mécaniques de la chènevotte, Travail de fin d'études, ENTPE 155 (2008) 2008.

[28] P. Łapka, F. Dietrich, P. Furmański, M. Sinka, G. Sahmenko, D. Bajare, Experimental and numerical estimation of thermal conductivity of bio-based building composite materials with an enhanced thermal capacity, Journal of Energy Storage 97 (2024) 112943.

[29] S. Tulip, N. Sarker, N. Nahar, M. Yang, E. Monono, Effect of Process Parameters on the Physical and Mechanical Properties of Cornstarch-Based Construction Materials, Construction Materials 3(3) (2023) 320-336.

[30] H. Song, T. Kim, A. Hajimohammadi, J.E. Oh, A. Castel, Detailed characterisation of hemp and hempcrete pore structures: Effects on thermal and acoustic properties, Cement and Concrete Research 186 (2024) 107702.

[31] S.N. Kabekkodu, J. Faber, T. Fawcett, New Powder Diffraction File (PDF-4) in relational database format: advantages and data-mining capabilities, Acta Crystallographica Section B: Structural Science 58(3) (2002) 333-337.

[32] Z. Yao, A. Kashani, A. Rawal, H. Song, T. Kim, Heat-induced phase transitions in mining tailings to create alternative supplementary cementitious materials, Resources, Conservation and Recycling 210 (2024) 107818.

[33] P. Tronet, T. Lecompte, V. Picandet, C. Baley, Study of lime hemp concrete (LHC)–Mix design, casting process and mechanical behaviour, Cement and Concrete Composites 67 (2016) 60-72.

[34] U. Dhakal, U. Berardi, M. Gorgolewski, R. Richman, Hygrothermal performance of hempcrete for Ontario (Canada) buildings, Journal of cleaner production 142 (2017) 3655-3664.

[35] W. Dai, Y. Gan, Measurement of effective thermal conductivity of compacted granular media by the transient plane source technique, EPJ Web of Conferences, EDP Sciences, 2017, p. 02016.

[36] F. Delhomme, A. Castel, A. Almeida, C. Jiang, D. Moreau, Y. Gan, X. Wang, S. Wilkinson, Mechanical, acoustic and thermal performances of Australian hempcretes, CIGOS 2021, Emerging Technologies and Applications for Green Infrastructure: Proceedings of the 6th International Conference on Geotechnics, Civil Engineering and Structures, Springer, 2022, pp. 753-761.

[37] P. de Bruijn, P. Johansson, Moisture fixation and thermal properties of lime–hemp concrete, Construction and Building Materials 47 (2013) 1235-1242.

[38] F. Benmahiddine, F. Bennai, R. Cherif, R. Belarbi, A. Tahakourt, K. Abahri, Experimental investigation on the influence of immersion/drying cycles on the hygrothermal and mechanical properties of hemp concrete, Journal of Building Engineering 32 (2020) 101758.

[39] X. Zhao, Y. Liu, L. Zhao, A. Yazdkhasti, Y. Mao, A.P. Siciliano, J. Dai, S. Jing, H. Xie, Z. Li, A scalable high-porosity wood for sound absorption and thermal insulation, Nature Sustainability 6(3) (2023) 306-315.

[40] R. Yang, C. Xu, Y. Lan, Y. Qiu, Z. Wang, Y. Peng, Q. Zeng, Near pixel-level characterisation of microfibres in 3D-printed cementitious composites and migration mechanisms using a novel iterative method, Composites Part A: Applied Science and Manufacturing 186 (2024) 108404.

[41] S. Dartois, S. Mom, H. Dumontet, A.B. Hamida, An iterative micromechanical modeling to estimate the thermal and mechanical properties of polydisperse composites with platy particles: Application to anisotropic hemp and lime concretes, Construction and Building Materials 152 (2017) 661-671.

[42] Y. Hamada, W. Otsu, J. Fukai, Y. Morozumi, O. Miyatake, Anisotropic heat transfer in composites based on high-thermal conductive carbon fibers, Energy 30(2-4) (2005) 221-233.

[43] A.P. Manian, M. Cordin, T. Pham, Extraction of cellulose fibers from flax and hemp: a review, Cellulose 28(13) (2021) 8275-8294.

[44] N. Mokshina, T. Chernova, D. Galinousky, O. Gorshkov, T. Gorshkova, Key stages of fiber development as determinants of bast fiber yield and quality, Fibers 6(2) (2018) 20.

[45] X. Yang, W. Zhu, Q. Yang, The viscosity properties of sodium silicate solutions, Journal of Solution Chemistry 37 (2008) 73-83.

[46] M.R. Ahmad, B. Chen, M.A. Haque, S.M.S. Kazmi, M.J. Munir, Development of plant-concrete composites containing pretreated corn stalk bio-aggregates and different type of binders, Cement and Concrete Composites 121 (2021) 104054.

[47] C. Narattha, S. Wattanasiriwech, D. Wattanasiriwech, Thermal and mechanical characterization of fly ash geopolymer with aluminium chloride and potassium hydroxide treated hemp shiv lightweight aggregate, Construction and Building Materials 331 (2022) 127206.

[48] X. Zhao, A.H. Brozena, L. Hu, Critical roles of pores and moisture in sustainable nanocellulose-based super-thermal insulators, Matter 4(3) (2021) 769-772.

[49] H. Liu, X. Zhao, Thermal conductivity analysis of high porosity structures with open and closed pores, International Journal of Heat and Mass Transfer 183 (2022) 122089.

[50] S. Amziane, F. Collet, M. Lawrence, C. Magniont, V. Picandet, M. Sonebi, Recommendation of the RILEM TC 236-BBM: characterisation testing of hemp shiv to determine the initial water content, water absorption, dry density, particle size distribution and thermal conductivity, Materials and Structures 50(3) (2017) 167.

<Highlights>

- 3D hempcrete phases and hemp shives properties were analysed using micro-computed tomography
- Hempcrete with alkaline-activated binder showed improved strength and thermal conductivity
- Alkali activated binder led to denser mortar matrix with small and horizontally aligned hemp shives

Declaration of interests

☒ The authors declare that they have no known competing financial interests or personal relationships that could have appeared to influence the work reported in this paper.

☐ The authors declare the following financial interests/personal relationships which may be considered as potential competing interests: